Journal of *Marine Science and Engineering*

MDPI

Article

Experimental Study of the Combined Action of Random Waves and Current Induced Hydrodynamics and Seabed Response Around a Protective Three-Dimensional Pipeline

Dayu Chang [1], Risheng Wang [1], Wenqi Si [1], Mengxiao Li [2], Zheng Wang [2], Dajun Liu [3], Ke Sun [1,*], Dong-Sheng Jeng [2,4], Lin Cui [2] and Dejian Wei [5]

[1] College of Transportation and Civil Engineering, Shandong Jiaotong University, Jinan 250357, China; changdayu7@gmail.com (D.C.); 204055@sdjtu.edu.cn (R.W.); 19861836034@163.com (W.S.)
[2] College of Civil Engineering, Qingdao University of Technology, Qingdao 266033, China; lmx000710@163.com (M.L.); 19715329861@163.com (Z.W.); d.jeng@griffth.edu.au (D.-S.J.); cuilin@qut.edu.cn (L.C.)
[3] School of Marine Sciences, Guangxi University, Nanning 530003, China; 2327301013@st.gxu.edu.cn
[4] School of Engineering & Built Environment, Griffith University Gold Coast Campus, Southport, QLD 4222, Australia
[5] Pinglu Canal Group Co., Ltd., Nanning 530201, China; plyhkjxxb@163.com
* Correspondence: 210114@sdjtu.edu.cn

Abstract

Submarine pipelines serve as the primary transportation infrastructure for offshore energy resources and are becoming increasingly important in modern industrial and domestic applications. A series of laboratory experiments on the dynamic seabed response of three-dimensional pipeline-seabed systems under random wave and current conditions was conducted. The results demonstrate as follows: (1) Under the combined action of random waves and ambient currents, the wave profiles in the vicinity of the submarine pipeline exhibit distinct irregular and nonlinear characteristics; (2) Compared with random waves acting alone, the superposition of random waves and currents modifies wave propagation behavior: a co-directional current enhances wave propagation, whereas a countercurrent suppresses it; (3) For a pipeline subjected to the three-dimensional random waves, pore-pressure amplitude decreases with increasing wave-incidence angle. Specifically, maximum values corresponding to incidence angles of 30° and 45° are generally lower than those at 0° and 15°, at a seabed depth of z/d = 0.0938, and the value at an incident angle of 45 degrees attenuates by 21.31% compared to that of 0°; (4) Coarse sand exhibits weaker pore-pressure attenuation than fine sand around the three-dimensional pipeline-seabed scheme, indicating that sediment grain size exerts a substantial influence on seabed response; (5) The protective effect of geotextile and stone is more obvious, whereas PVC is limited to the front and underside of the pipe. The deeper the seabed, the smaller the effect of protective measures. For reproducibility, the test matrix covered wave-incidence angles α = 0°, 15°, 30°, and 45°, irregular-wave conditions with $H_{1/3}$ = 0.08–0.14 m and $T_{1/3}$ = 1.2–1.8 s, and currents U = –0.2 m/s at a constant still-water depth h = 0.45 m.

Keywords: three-dimensional pipeline; oblique random wave; oscillation pore pressure; hydrodynamics; wave flume experiment

Check for updates

Academic Editor: Weicheng Cui

Received: 2 January 2026
Revised: 2 February 2026
Accepted: 25 February 2026
Published: 1 March 2026

Copyright: © 2026 by the authors. Licensee MDPI, Basel, Switzerland. This article is an open access article distributed under the terms and conditions of the Creative Commons Attribution (CC BY) license.

1. Introduction

With the continued expansion of offshore oil and gas development, subsea pipelines have become indispensable components of marine energy-transportation systems. However, the intense wave and current actions in coastal environments can significantly alter the pressure and velocity fields around pipelines [1], inducing pore-pressure response, seabed liquefaction, local scour, and even structural instability—factors that have repeatedly been identified as major mechanisms responsible for subsea pipeline failures [2,3]. Consequently, understanding the dynamic response of the pipeline–seabed system under combined wave–current loading is essential for the safe design of submarine pipelines.

Previous studies worldwide have predominantly focused on two-dimensional (2D) wave/current–pipeline–seabed coupled systems, employing experimental observations and numerical simulations to reveal a series of key mechanisms. For instance, 2D experimental investigations have shown that wave period, wave height and current velocity directly influence both the amplitude of pore-water pressure and its attenuation with depth around the pipeline [4,5]. Additional studies further demonstrated that soil saturation, permeability, and pipeline burial depth can markedly modify the extent of seabed liquefaction as well as stress-propagation pathways [6–8]. Ke Sun et al. [9] conducted laboratory experiments on wave propagation over partially buried pipelines in a flume, while Yuan Gao et al. [10] examined the seabed response of silty soils surrounding trench-type pipelines under wave action. These experimental findings have provided an important foundation for understanding pipeline dynamics under regular waves or simple wave–current superposition.

In parallel, 2D numerical simulations have played a dominant role in wave–current–seabed coupling research. Utilizing Biot's dynamic consolidation theory, VOF-based wave models, and CFD–pyroclastic coupling methods, numerous studies have successfully simulated wave-induced pore-pressure transmission, the influence of pipeline embedment or span on seabed response, and nonlinear hydrodynamic variations under combined wave–current action [11,12]. For example, Liu Xiaoli et al. (2021) [13] investigated the characteristics and mechanisms of seabed response around buried pipelines while incorporating cumulative pore pressure and stress-coupling effects. These 2D numerical models are capable of reproducing hydrodynamic responses and seabed behaviors under regular wave conditions, and are therefore widely used in engineering practice.

Beyond the pipeline-specific literature, recent studies on other marine energy and floating systems consistently show that hydrodynamic performance and structural response can be highly sensitive to (i) geometric/configurational parameters and (ii) sea-state characteristics, even when the governing forcing is nominally similar. For instance, a numerical investigation of cross-flow Savonius turbines reported pronounced sensitivity to immersion depth and rotation direction, implying that geometry and operational settings can substantially alter vortex structures and load-transfer pathways [14]. Likewise, CFD-based seakeeping analyses of floating photovoltaic platforms (semi-submersible versus catamaran concepts) under irregular JONSWAP seas demonstrated that motion responses (e.g., heave, roll, pitch) vary markedly with both sea-state spectra and platform configuration [15]. Taken together, these findings support the central premise of this study: for submarine pipelines, oblique incidence and protection-layer configuration are expected to modulate the near-field hydrodynamic loading and thus the coupled seabed pore-pressure response, motivating the present 3D flume experiments.

However, real marine environments are inherently directional and three-dimensional, featuring oblique wave incidence and broadband irregular energy distributed over frequency and direction. In contrast, most large-scale wave flumes generate predominantly unidirectional irregular waves. Therefore, laboratory investigations that seek to represent

oblique incidence in a flume typically adopt an effective oblique-incidence configuration (e.g., by rotating the structure relative to the wave-propagation axis), rather than reproducing a fully multi-directional, multi-component directional sea state. This distinction is important when interpreting "3D" effects reported from flume experiments. Here, "3D" refers to oblique-incidence wave/current loading that induces spanwise (along-pipe) flow components and pressure/pore-pressure gradients around the pipeline. Because the flume wavemaker generates plane waves in a single direction, the experiment does not reproduce full directional-spreading sea states; this limitation is stated explicitly in Section 2.1.

In the 3D direction, numerical simulation has advanced more rapidly. Yu Peng et al. [16] established a fully coupled 3D wave–current–seabed–pipeline numerical model—including wave generation, hydrodynamic computation, and sediment-transport modules—to examine how water depth, flow velocity, and pipeline span influence the evolution of 3D local scour. Zhu Fu et al. [17] analyzed the three-dimensional distribution and controlling factors of local scour and sediment deposition around practical subsea pipelines, providing valuable methodologies and case studies for engineering-oriented 3D numerical simulations. Moreover, a number of scholars have developed 3D CFD-based coupled wave–seabed–pipeline models to systematically investigate the effects of wave-incidence angle, random wave spectra, pipeline burial depth, and soil properties on 3D pore-pressure distribution and liquefaction patterns [18–22]. These models successfully capture asymmetric pressure differences between the upstream and downstream sides of the pipeline, the spatial evolution of 3D vortical structures, and the propagation characteristics of random-wave energy, highlighting the advantages of 3D approaches. Furthermore, high-fidelity 3D models—such as those utilizing high-order RANS formulations, LES turbulence simulations, or fully 3D numerical wave tanks—have noticeably improved the accuracy of wave–current–pipeline–seabed coupling research [23].

Despite the rapid progress in numerical simulations, 3D physical experiments remain scarce. Due to constraints such as flume dimensions, measurement challenges, and experimental complexity, existing 3D experiments have mainly focused on regular waves or simple wave–current combinations, addressing topics such as pipeline protection, scour patterns, or local pressure variations [24–26]. At present, there is virtually no systematic body of experimental data specifically addressing 3D pipeline–seabed dynamic responses under random waves, and measurements involving oblique incidence, multidirectional wave–current conditions, and random wave spectra are particularly lacking. Therefore, developing 3D experimental systems and conducting corresponding experiments is crucial for validating 3D numerical models, refining engineering design formulations, and improving the accuracy of offshore pipeline stability assessments.

Novelty and new insights compared with prior 2D studies. Unlike conventional 2D flume/sectional studies that assume normal wave incidence and spanwise-uniform loading, this work provides a physical dataset for an obliquely loaded 3D pipeline-seabed system under irregular (JONSWAP) waves combined with steady current, quantification of how an effective wave-incidence angle (0–45°) modifies circumferential wave pressure and the spatial attenuation of oscillatory pore pressure, and an experimental comparison of three protection schemes (none/geotextile-stone/PVC cover) in the same hydrodynamic forcing, which is rarely available for validating 3D numerical models and design guidance.

Research gap, approach, and measurable objectives. The key gap is the lack of systematic laboratory measurements for 3D pipeline-seabed responses under oblique-incidence irregular waves with co- and counter-directional currents, especially with protection measures. To address this, we conduct synchronized measurements of free-surface elevation, circumferential wave pressure, and seabed pore pressure for four effective incidence angles. The study pursues three measurable objectives: quantify wave profile distortion and

circumferential wave-pressure amplification around the pipeline as functions of $H_{1/3}$, $T_{1/3}$, U and α; characterize the depthwise attenuation/phase lag of oscillatory pore pressure for two sands (d_{50} = 0.2037 and 0.3078 mm) and identify the sensitivity to α and U; evaluate and compare the pore-pressure mitigation performance of geotextile-stone and PVC protection relative to the unprotected case.

In recent years, growing attention has been directed toward the influence of soil–pipe interaction and pore-water pressure on the stability of submarine pipeline protection systems. Under dynamic loads such as waves, currents, and earthquakes, fluctuations in seabed pore-water pressure can sharply reduce effective stress, induce soil liquefaction, and consequently trigger pipeline settlement, uplift, lateral displacement, or overall instability. Numerical analyses by Mengyu Lin et al. [27], based on Biot's consolidation theory coupled with the finite element method, demonstrated that soil permeability and elastic modulus are critical parameters governing pore-pressure transmission and the magnitude of seepage forces acting on buried pipelines; in dense or low-permeability sands, the slow dissipation of pore pressure generates significant vertical gradients that can impose strong vertical seepage forces, thereby increasing the likelihood of pipeline uplift or settlement. Experimental comparisons conducted by Wenqi Si et al. [24] further showed that the application of protective layers under combined wave–current action substantially reduces the pore-pressure amplitude in the soil surrounding and beneath pipelines, slows the vertical attenuation of pore pressure, and effectively suppresses seabed liquefaction, ultimately enhancing pipeline stability. In addition, S. Neelamani et al. [28] proposed a method for estimating optimal burial depth by integrating soil type with hydrodynamic and wave–current conditions, underscoring the importance of pore-pressure behavior and wave–soil interaction in burial-depth design. Collectively, these findings highlight the necessity of fully accounting for pore-pressure variations in submarine pipeline protection design, as such analyses not only support the evaluation of liquefaction risks and potential pipeline uplift or settlement but also provide a theoretical basis for determining protection strategies and burial configurations, which will be further examined in this study through integrated numerical and experimental investigation.

The installation of geotextile and stone protective layers around a three-dimensional submarine pipeline can markedly alter the temporal and spatial characteristics of seabed pore water pressure under combined wave–current action. As a flexible protective material with high permeability and low stiffness, geotextile effectively filters fine particles and attenuates the direct transmission of wave-induced pressure at the seabed surface, thereby reducing the pore water pressure amplitude at the upstream side and beneath the pipeline, while suppressing rapid pore pressure buildup and delayed dissipation. In contrast, stone protection increases the surface roughness and overall stiffness of the seabed, enhancing wave–current energy dissipation and reflection and forming a pronounced wave-dissipation zone in front of the pipeline. Consequently, the pore water pressure exhibits stronger attenuation in both horizontal and vertical directions. Overall, geotextile protection is more effective in improving the seepage stability of the shallow seabed in the vicinity of the pipeline, whereas stone protection plays a more dominant role in reducing the overall pore pressure response and enhancing resistance to scour. Both protective measures significantly contribute to improving the operational safety of three-dimensional submarine pipelines in complex wave–current environments [29,30].

Given this premise, the present study performs laboratory experiments under combined current and unidirectional irregular waves, while realizing an effective oblique-incidence condition by rotating the pipeline relative to the wave-propagation direction. Accordingly, the term "3D" in this paper refers to the three-dimensionality of the near-field hydrodynamic and seabed response around the pipeline under oblique incidence, rather

than to a fully directional wave field. The study quantifies how the effective incidence angle and protective measures modulate free-surface evolution, circumferential dynamic pressure on the pipeline, and the spatial attenuation and phase characteristics of pore-pressure response in the sandy seabed.

2. Laboratory Experiment Setup

2.1. Experimental Setup

The experimental study was conducted in a large wave flume with internal dimensions of 50.0 m in length, 1.2 m in width, and 1.3 m in depth, as shown in Figure 1. The sidewalls of the flume were constructed of transparent plexiglass to facilitate flow visualization, while the bottom was composed of a rigid, impermeable reinforced concrete material. A concrete sandpit (3.6 m × 1.2 m × 0.32 m) was installed between two concrete slopes (each 3.15 m long with a slope ratio of 1:10), positioned 21.7 m downstream away from the wave generator.

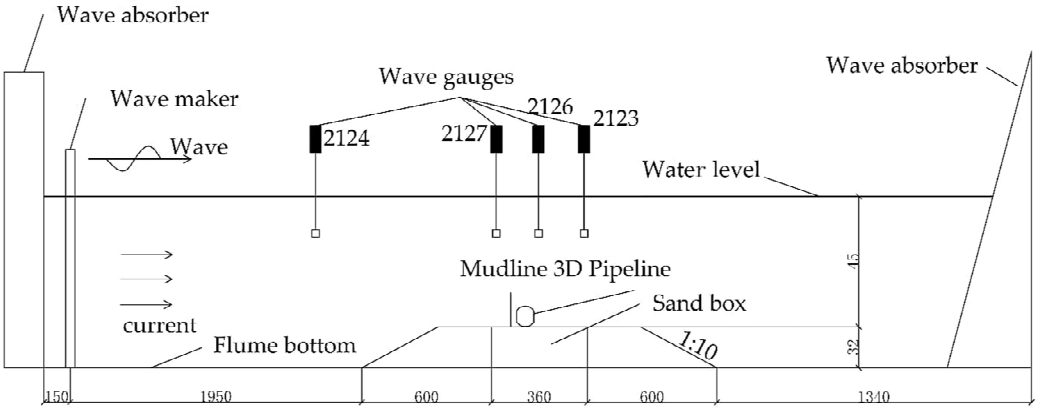


Figure 1. Experiment setup (Unit: mm): The flume generates predominantly unidirectional irregular waves. Oblique incidence is represented by rotating the pipeline by an angle α with respect to the wave-propagation axis, yielding an effective oblique-incidence loading condition rather than a fully multi-directional sea.

A hydraulic piston-type wavemaker was installed at the upstream end of the flume, while a sponge-layer wave absorber was placed at the downstream end to dissipate the incident wave energy and minimize wave reflection. The absorption system is installed on an inclined ramp of slope 1:1. The effective wave reflection coefficient Kr measured by the two-point method (using WHG2123 and WHG2127 equipment produced by Shengying Co. Ltd., Chengdu, China, following the standard reflection analysis procedure) in this test tank is 0.25. This configuration was adopted to minimize standing-wave contamination in the sandpit region. The wave-generation system was capable of producing both regular and irregular waves, accompanied by or without unidirectional flow conditions. The wavemaker was capable of generating waves with heights ranging from 0 to 0.25 m, periods between 1.0 and 4.0 s, and water depths from 0.1 to 1.0 m. By manually adjusting the inverter settings, a bi-directional steady flow field could be generated to simulate current. The steady reversible flow velocity could reach up to 0.3 m/s. Throughout all experimental runs, the still water depth was maintained at 0.45 m.

To ensure that the reported wave–current loading and seabed pore-pressure responses are not biased by facility artifacts, three quality-control checks were conducted. (1) Wave absorption and reflection: The residual reflection level was quantified using a multi-gauge separation method in the test section, and the reflection coefficient was confirmed to remain below $C_r \leq 0.10$ for the target irregular-wave cases; the gauge spacing and analysis window

are reported to ensure reproducibility. (2) Current uniformity: The imposed steady current was verified to be laterally and vertically uniform over the pipeline influence region by cross-sectional velocity profiling, showing that the spatial non-uniformity was within ±5% of the set value. (3) Sidewall and oblique-alignment effects: Given the finite flume width (B = 1.2 m, i.e., $D/B \approx 0.083$) and the oblique pipeline orientation used to represent an effective incidence angle, potential wall-induced asymmetry and blockage effects were evaluated by comparing symmetric measurement locations and repeating a subset of runs with a shifted lateral position; the resulting deviation in key hydrodynamic metrics (e.g., peak or RMS pressure) was within 5% for $\alpha \leq 45$. Collectively, these checks support that the observed trends in wave pressure and pore-pressure attenuation primarily reflect the intended variations in incidence angle and protection configuration, rather than reflections, flow non-uniformity, or wall effects.

Given that the experimental wave tank is capable of generating waves only along a single propagation direction, whereas waves in real marine environments are inherently multi-directional and span a wide range of incident angles, an adjustment was introduced to better approximate realistic sea states. Specifically, the incident angle of waves acting on the pipeline was varied by rotating the pipeline model relative to the direction of wave propagation. In this study, four incident angles were configured, namely α = 0°, 15°, 30°, and 45°. Correspondingly, pipeline models were designed according to both the interior width of the wave tank and the prescribed incident angles. The detailed spatial arrangements of the four pipeline configurations used in the experiment are presented in Figure 2. By rotating the pipeline, the incident-wave vector contains a component parallel to the pipe axis, which produces along-pipe (spanwise) variations in the near-bed velocity field and asymmetric pressure distributions. The resulting hydrodynamics and seepage response are therefore three-dimensional in the local pipe vicinity, even though the incoming wave field itself is nominally planar. All pore-pressure and wave-pressure measurements were taken near the pipe midspan to minimize end-wall effects and to capture the representative quasi-3D response. All wave-pressure and pore-pressure sensors were located close to the pipe midspan; with a 0.01-m gap between the pipeline and each side wall (as described in Section 2.3), this ensures that end-wall constraints do not dominate the measured local 3D response.



(**a**)

Figure 2. *Cont.*



Figure 2. Physical drawing of the model pipe arrangement: (**a**) Model pipeline layout at wave (flow) incident angle $\alpha = 0°$; (**b**) Model pipeline layout at wave (flow) incident angle $\alpha = 15°$; (**c**) Model pipeline layout at wave (flow) incident angle $\alpha = 30°$; (**d**) Model pipeline layout at wave (flow) incident angle $\alpha = 45°$.

2.2. Measuring Instruments

In the physical model experiments, a suite of high-precision instruments was employed to obtain synchronized measurements of free-surface elevation, wave pressure, and pore pressure around the pipeline, as illustrated in Figure 3. The measurement system comprised four wave height gauges (WHG2123, WHG2124, WHG2126, and WHG2127 produced by Shengying Co., Ltd., Chengdu, China), eight wave pressure transducers (Pw1–Pw8), and twelve pore pressure sensors (P_{ij}, i = 1–4, j = 1–3).

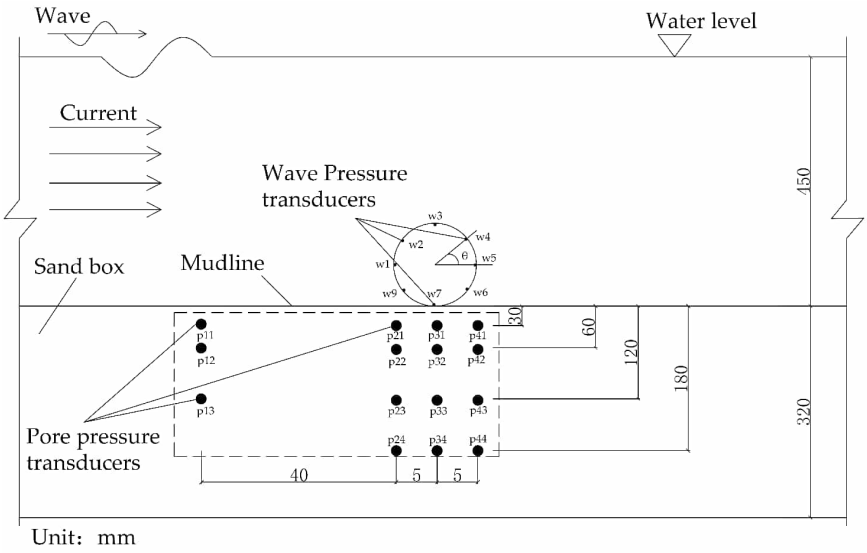


Figure 3. Locations of wave-pressure transducers and pore-pressure transducers.

The wave height gauges (model YWH203-D, Nanjing Intelligent Technology Co., Ltd., Nanjing, China) had a measurement range of 0–0.60 m and an accuracy of ±0.15%, and were used to continuously monitor variations versus time in the free-surface elevation. Among them, WHG2124 served as a far-field reference gauge positioned 7.8 m upstream from the pipeline center to record the incident wave characteristics. The remaining three gauges (WHG2123, WHG2126, and WHG2127) were installed 1.8 m upstream, directly above, and 1.8 m downstream of the pipeline center, respectively, capturing the spatial evolution of wave profiles and assess wave–structure–seabed interactions. Prior to each test series, all gauges were calibrated under still-water conditions by incrementally adjusting the water level to 10 known elevations spanning the full measurement range (typically 0.00 to 0.30 m) and recording the corresponding voltage output. A linear regression was then applied to obtain the calibration coefficient (sensitivity) and offset for each gauge. The calibration quality was quantified by the coefficient of determination ($R^2 \geq 0.999$) and the standard deviation of the regression residuals ($\sigma_{cal} \leq 0.3$ mm). The measurement uncertainty of free-surface elevation was evaluated following standard uncertainty propagation, including contributions from the reference water-level setting (±0.5 mm), the electronic noise estimated from the still-water time series (standard deviation $\sigma_{noise} \leq 0.2$ mm), and the calibration fit residuals (σ_{cal}). The combined standard uncertainty was calculated as $u_\eta = \sqrt{u_{ref}^2 + \sigma_{noise}^2 + \sigma_{cal}^2}$, and the expanded uncertainty was reported with a coverage factor $k = 2$, yielding $U_\eta \approx \pm 1.2$ mm for wave elevation measurements. After calibration, a zero-check was conducted before and after each run to confirm negligible drift (≤0.5 mm), ensuring the repeatability and traceability of the wave gauge readings.

Wave-induced pore-water pressures were measured using miniature intelligent pressure transducers developed by Chengdu Keda Shengying Co., Ltd, Chengdu, China. Specifically, eight CY302 sensors (range: 0–20 kPa, accuracy: ±0.1%, outer diameter: 6 mm) were used for wave pressure measurements, while fifteen CY303 sensors (range: 0–30 kPa, accuracy: ±0.1%, outer diameter: 8 mm) were embedded in the seabed to record pore pressure variations. The CY302 transducers were uniformly distributed around the pipeline periphery at angular intervals of $\pi/4$. Each sensor probe was passed through the pipeline wall and fixed securely using sealing tape, ensuring the sensing surface was flush with the outer surface of the pipe. The pore pressure transducers (P_{ij}) were buried at four cross-sections and three different depths within the sand bed, as shown in Figure 3, where i represents the cross-section number and j denotes the embedment depth. The

numbering was arranged according to the direction of wave propagation (from left to right). All pore-pressure transducers and wave-pressure gauges were calibrated prior to the experimental campaign and re-checked after the test series to quantify drift. Calibration was performed using a hydrostatic water-column method that generated reference pressures p_{ref} = ρgh spanning 0–20 kPa, covering at least 90% of the sensor's full-scale range. For each sensor, a linear regression between the recorded output and p_{ref} was established, yielding a sensitivity of (0.8–1.2) [unit]/kPa with a coefficient of determination $R^2 \geq 0.999$. The maximum nonlinearity and hysteresis were controlled within 0.5%FS and 0.3%FS, respectively. The combined standard uncertainty was evaluated following GUM by propagating contributions from reference head reading uncertainty (±1 mm, equivalent to ±0.01 kPa), density/temperature variability (±0.02 kPa), repeatability and electronic noise during static holds (0.05 kPa, 1σ), and (iv) regression residuals (0.05 kPa). The resulting expanded uncertainty (k = 2) was ±0.30 kPa for pore-pressure measurements and ±0.50 kPa for wave-pressure measurements. Zero-offset drift assessed from pre-/post-run static readings remained within 0.5%FS, and baseline corrections were applied when required.

All signals from the wave gauges, wave pressure sensors, and pore pressure sensors were simultaneously sampled at 100 Hz using a remote computer system connected to both the servo control unit and the data acquisition system, ensuring precise synchronization of all measurements. The experimental scale is chosen as 1:50. The model pipe outer diameter D = 0.10 m and still-water depth h = 0.45 m were selected to satisfy geometric constraints of the flume while preserving key non-dimensional similarity parameters governing wave–structure interaction. With the adopted geometric scale of 1:50, the corresponding prototype values are Dp = 5 m and hp = 22.5 m. The target ratio h/D = 4.5 (prototype h/D ≈ 4.5) is representative of nearshore/trench pipeline conditions.

Measurement uncertainty, calibration, sampling adequacy, and drift control. Prior to each test series, the wave gauges and pressure transducers (wave pressure and pore-pressure sensors) were calibrated using a static water-level procedure and a hydrostatic pressure-column method, respectively, yielding linear calibration curves with coefficients of determination $R^2 \geq 0.999$. To ensure sampling adequacy, the acquisition frequency (100 Hz) provides approximately 120–180 samples per dominant wave period for the tested irregular-wave conditions (dominant period T_p = 1.2–1.8 s), which is sufficient to resolve the pressure and pore-pressure fluctuations without temporal aliasing; where necessary, an anti-aliasing low-pass filter with a cut-off frequency of 20 Hz was applied prior to analysis. Potential signal drift was monitored by recording pre- and post-test baseline segments of duration 60 s under quiescent conditions; the drift magnitude was constrained within 0.5 kPa and corrected by baseline detrending when exceeded. Based on calibration uncertainty, sensor resolution, and repeatability from repeated runs (n = 3), the expanded uncertainties (k = 2) are estimated as ±0.001 m for wave elevation, ±0.5 kPa for dynamic wave pressure, and ±0.5 kPa for pore-water pressure. These quality-control steps provide quantitative confidence bounds for the trends reported in Section 3.

The flume test is based on the following criteria for Froude number:

$$\lambda = \frac{\lambda_{u_m}}{\lambda_g^{\frac{1}{2}} \lambda_g^{\frac{1}{2}}} \tag{1}$$

where λ_g = 1, we can obtain the following:

$$\lambda_{u_m} = \lambda_{D^{\frac{1}{2}}} \tag{2}$$

$$\lambda_T = \frac{\lambda_D}{\lambda_{u_m}} = \lambda_{D^{\frac{1}{2}}} \tag{3}$$

$$\lambda_{KC} = \frac{\lambda_{u_m}\lambda_T}{\lambda_D} = 1 \quad (4)$$

The above derivation shows that the flume test can satisfy the requirements for both the Fr and KC values.

Under a fixed geometric scale, it is generally not possible to satisfy Reynolds-number similarity simultaneously with Froude similarity in laboratory flumes. This is a well-known constraint in hydraulic modeling: once the velocity scale is set by Froude similarity, matching Reynolds similarity would require an incompatible adjustment of viscosity or length scale. In this study, the experiments are conducted in a regime where the flow around the pipe and over the seabed is predominantly inertia-dominated, so viscous effects are expected to be secondary and mainly confined to near-boundary layers. Therefore, the interpretation of hydrodynamic loading focuses on inertia–gravity forcing and wave–current interaction, while acknowledging that small-scale viscous effects may influence detailed turbulence characteristics.

For the porous sandy seabed, the pore-pressure response is influenced not only by external hydrodynamic loading but also by hydraulic diffusion within the sediment, which depends on permeability and compressibility. Exact similitude of seabed response would require preserving permeability-related non-dimensional parameters (e.g., ratios comparing diffusion timescales to wave-period timescales), which cannot be perfectly matched concurrently with Froude and KC similarity in a practical physical model. Accordingly, the present results are interpreted as revealing robust relative trends—such as the sensitivity to wave randomness, current, effective oblique incidence angle, and protection measures—rather than providing a direct one-to-one extrapolation of absolute prototype pore-pressure amplitudes. This positioning clarifies the role of scale effects and strengthens the validity of comparative conclusions drawn within the tested parameter space.

2.3. Quality of Samples

The seabed material used in the experiments consisted of sand with a median grain size of d_{50} = 0.2037 mm and d_{50} = 0.3078 mm, and its primary physical properties are summarized in Table 1. The grain size distribution of the model sand was determined through sieve analysis, and the resulting grading curve is presented in Figure 4. The permeability coefficient of the sand was obtained using a constant-head permeability test conducted under laboratory conditions. For each sediment type (fine sand and coarse sand), representative samples were collected from the bulk material, oven-dried to constant mass, and mechanically sieved through a graded stack of sieves with mesh openings spanning the target size range. The cumulative grain-size distribution curve was then constructed, from which characteristic diameters and the uniformity coefficient $C_u = d_{60}/d_{10}$ were obtained. To ensure repeatability, the sieve test was repeated three times for each sediment type, and the reported d_{50} values correspond to the mean of the repeats with a relative deviation within $\pm 2\%$. Prior to placement in the flume, the sediment was thoroughly mixed to minimize segregation; after placement, the bed was gently leveled, and the local thickness in the vicinity of the pipe was checked at multiple locations to confirm uniformity. In addition, because rock- or gravel-based protection layers may introduce a different length scale than sand, the geometric similarity of any protective aggregates was evaluated using the dimensionless size ratio and reported together with the grain-size statistics. This approach ensures that the adopted sediment and protective-material sizes are objectively characterized and that potential scale effects associated with particle size are explicitly addressed. Throughout all test runs, the seabed thickness was consistently maintained at 0.45 m.

Table 1. Soil Characteristics.

Parameters	Notation	Values	
		Sample 1	Sample 2
Average particle size	d_{50} (mm)	0.2037	0.3078
Dry density	ρ_d (g/cm^3)	1.5337	1.5026
Maximum dry density	ρ_{dmax} (g/cm^3)	1.6076	1.5785
Minimum dry density	ρ_{dmin} (g/cm^3)	1.2963	1.2500
Specific gravity	G_s (g/cm^3)	2.6540	2.6549
Permeability coefficient	k_s (cm/s)	0.0767	0.2991
Shear modulus	G (MN/m^2)	9.23	12.69
Poisson's ratio	μ	0.30	0.30
Porosity	n	0.4221	0.4340
Void ratio	e	0.7304	0.7669
Relative density	D_r	0.7994	0.8077

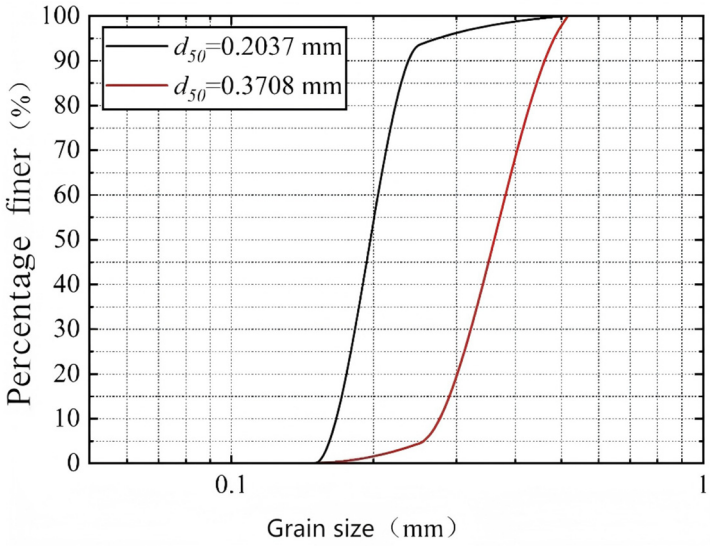


Figure 4. Grade distribution diagram.

A polyvinyl chloride (PVC) pipe with an outer diameter (D) of 0.10 m and a wall thickness of 0.01 m was employed as the model pipeline. The pipe was installed on the seabed either perpendicular or inclined relative to the direction of wave propagation. To minimize boundary effects, the pipe length was set to 1.19 m, slightly less than the internal width of the flume. Experimental observations indicated that the small clearance (0.01 m) between the pipe ends and the flume sidewalls introduced negligible disturbance to the surrounding flow field, thereby ensuring that end effects were negligible and that measurements near the pipe midspan were representative of the nominal 3D wave/current–seabed–pipe interaction. During all tests, the pipe was rigidly fixed within a custom-designed steel support frame, effectively preventing any translation or rotation of the pipeline throughout the experiments.

Two protective measures were adopted in the pipeline protection tests. The first involves a geotextile–stone cover system. The geotextile was cut into a rectangular sheet measuring 1.2 m in length and 0.2 m in width to ensure close adherence to the pipe surface. To prevent damage to the wave-pressure sensor probes mounted on the pipeline, flat pebbles with diameters of 3–8 cm were placed above the geotextile as a supporting framework, after which the voids were filled with black gravel (1.2–1.8 cm) to achieve complete coverage of the pipeline, as illustrated in Figure 5a. In practical engineering

applications, waste rock of various sizes can be utilized as a low-cost and environmentally sustainable protective material for submarine pipelines.

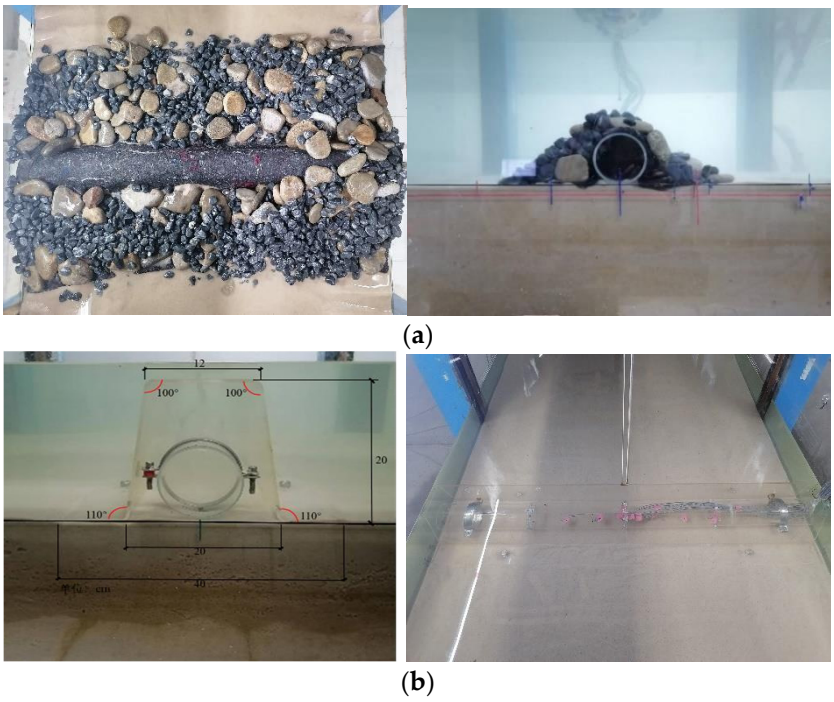


Figure 5. Diagram of the field setup of the pipeline protection test model. (**a**) geotextile–stone; (**b**) PVC.

The second protective measure employs a PVC shielding cover mounted directly above the pipeline. The PVC cover is fabricated from polyvinyl chloride and designed with a top width of 0.12 m and a height of 0.18 m. It is secured to the seabed using four specialized anchoring screws. The detailed configuration is shown in Figure 5b.

2.4. Experimental Test Conditions and Sequence

The experimental conditions are summarized in Table 2. The incident wave heights varied from 0.08 m to 0.14 m in increments of 0.02 m, while the wave periods ranged from 1.2 s to 1.8 s with an interval of 0.2 s. The steady current velocity was adjusted between −0.2 m/s and 0.2 m/s, where positive values denote currents in the same direction as wave propagation, and negative values indicate opposing currents. Detailed test conditions are listed in the following table. Note that the data shown in Table 2 were obtained under irregular wave conditions to more accurately simulate realistic marine environments. Key experimental parameters (all values in prototype scale are not used; the following are model-scale settings used in the flume): (i) still-water depth h = 0.45 m; (ii) pipeline outer diameter D = 0.10 m, wall thickness = 0.01 m, and pipe length L = 1.19 m; (iii) wave-incidence angles α = 0°, 15°, 30°, 45°; (iv) irregular waves: JONSWAP spectrum with γ = 3.3, significant wave height $H_{1/3}$ = 0.08–0.14 m ($\Delta H_{1/3}$ = 0.02 m) and significant period $T_{1/3}$ = 1.2–1.8 s ($\Delta T_{1/3}$ = 0.2 s); (v) combined wave–current tests: steady current velocity U = −0.2, 0.1, 0.2 m/s (negative denotes opposing current) plus U = 0 m/s reference; (vi) sampling frequency 100 Hz and record length ≥ 180 s per run; (vii) seabed thickness 0.45 m and two sands with d50 = 0.2037 mm and 0.3078 mm (Table 1). (v) current velocity U = −0.2, 0, 0.1, and 0.2 m/s (positive co-directional with waves); (vi) each run duration ≥ 180 s, sampling frequency 100 Hz for all sensors; (vii) seabed thickness 0.45 m with d50 = 0.2037 mm and 0.3078 mm; (viii) protective configurations: none, geotextile–stone

cover, and PVC cover (Figure 5). The JONSWAP spectrum was adopted for the generation of random waves, with the spectral density function as follows:

$$S(f) = \beta_J H_{1/3}^2 T_p^4 f^5 \exp[-1.25(T_p f)^{-4}] \gamma^{\exp[\frac{-(T_p f-1)^2}{2\sigma^2}]} \quad (5)$$

$$\beta_J = \frac{0.06238}{0.23 + 0.033\gamma - 0.185(1.9+\gamma)^{-1}} \times [1.094 - 0.01915 \mathrm{In}\gamma] \quad (6)$$

$$T_p = \frac{T_{1/3}}{1 - 0.132(\gamma + 0.2)^{-0.559}}, \sigma = \begin{cases} 0.07, f \le f_p \\ 0.09, f > f_p \end{cases} \quad (7)$$

Table 2. Irregular wave condition.

Test Conditions	Angle (°)	Wave Height $H_{1/3}$ (m)	Wave Period $T_{1/3}$ (s)	Current U (m/s)	Particle Size (mm)	Protective Measures
1	0	0.08	1.6	0	0.2037	Without
2		0.1	1.6	0		
3		0.12	1.6	0		
4		0.14	1.6	0		
5		0.1	1.2	0		
6		0.1	1.4	0		
7		0.1	1.8	0		
8		0.1	1.6	0.1		
9		0.1	1.6	0.2		
10		0.1	1.6	−0.2		
11		0.1	1.6	0	0.3078	
12	15	0.08	1.6	0	0.2037	
13		0.1	1.6	0		
14		0.12	1.6	0		
15		0.14	1.6	0		
16		0.1	1.2	0		
17		0.1	1.4	0		
18		0.1	1.8	0		
19		0.1	1.6	0.1		
20		0.1	1.6	0.2		
21		0.1	1.6	−0.2		
22		0.1	1.6	0	0.3078	
23	30	0.08	1.6	0	0.2037	
24		0.1	1.6	0		
25		0.12	1.6	0		
26		0.14	1.6	0		
27		0.1	1.2	0		
28		0.1	1.4	0		
29		0.1	1.8	0		
30		0.1	1.6	0.1		
31		0.1	1.6	0.2		
32		0.1	1.6	−0.2		
33		0.1	1.6	0	0.3078	

Table 2. *Cont.*

Test Conditions	Angle (°)	Wave Height $H_{1/3}$ (m)	Wave Period $T_{1/3}$ (s)	Current U (m/s)	Particle Size (mm)	Protective Measures
34	45	0.08	1.6	0	0.2037	Without
35		0.1	1.6	0		
36		0.12	1.6	0		
37		0.14	1.6	0		
38		0.1	1.2	0		
39		0.1	1.4	0		
40		0.1	1.8	0		
41		0.1	1.6	0.1		
42		0.1	1.6	0.2		
43		0.1	1.6	−0.2		
44		0.1	1.6	0	0.3078	
45	0	0.1	1.6	0	0.2037	Geotextile and stone PVC
46						

In the above formulation, T_p denotes the wave period associated with the spectral peak, whereas f_p represents the corresponding peak spectral frequency. The relationship between these two quantities is given by $T_p = \frac{1}{f_p}$. The parameter γ is the peak enhancement factor, which governs the sharpness of the JONSWAP spectral peak and typically varies within the range 1.0–7.0. In this study, a representative average value of γ = 3.3 is adopted.

The pipeline was tested under four inclination angles relative to the direction of wave propagation: 0°, 15°, 30°, and 45°. The following are all the groups of experiments in this paper.

The test procedure is as follows: To begin with, wave pressure sensors were installed inside the pipeline, and pore pressure sensors were fixed on a steel frame (Figure 3) before sand filling and soaked for 24 h to remove air. Wave gauges were arranged as in Figure 3, and the pipeline was fixed at 0°, 15°, 30°, and 45° relative to the wave direction. And then, Quartz sand was added to form the seabed, and the flume was filled with water to a depth of 0.45 m. During data collection, each run lasted at least 180 s, recording wave height, wave pressure, and pore pressure at 100 Hz. For regular waves, data recording stopped once steady conditions were reached; for combined wave–current tests, the wave and then current generators were shut down, followed by a 10–20 min rest period.

3. Results and Discussion

This study primarily investigates the variations in hydrodynamics around a subsea pipeline and the distribution of seabed pore pressure under oblique irregular waves with and without currents. Experimental observations were systematically compared at diverse angles of 0°, 15°, 30°, and 45° between the pipeline axis and the wave propagating direction. Furthermore, the role of soil particle size in controlling seabed pore water pressure is analyzed, and the comparative protective performance of geotextile and stone cover layers in mitigating pore water pressure around submarine pipelines is evaluated. In the experiments, the intersection of the seabed surface and the pipeline centerline was designated as the origin of coordinates, with the positive direction of the x-axis aligned with the direction of wave propagation and the positive z-axis direction extending upward from the seabed surface. In subsequent analyses, η represents the water profile, and $|p_w|$ denotes the maximum amplitude of the dynamic wave pressure. Additionally, the time-history variation curve of the pore-water pressure (p_s) was analyzed, as well as the distribution of seabed

pore pressure with depth under conventional wave-current interactions, and the variation patterns of pore pressure at different positions around the pipeline (forward, beneath, and backward). It should be noted that the pore pressure discussed here refers to excess pore pressure, which is obtained by subtracting the static pore pressure. Furthermore, to better visualize the changes in seabed pore pressure, the relevant data were non-dimensionalized. The equation $p_0 = \gamma_w \cdot h$ represents the static pore pressure at the seabed surface, where γ_w is the specific weight of water and h is the water depth. The effects of the soil property, i.e., median grain size of sediment particle, and random wave/current parameters such as wave height ($H_{1/3}$), wave period ($T_{1/3}$), and current velocity (U) on the distribution of seabed pore pressure around the pipeline were analyzed. Unless otherwise stated, the reported wave-elevation, dynamic-pressure, and pore-pressure statistics are interpreted together with the expanded measurement uncertainties (k = 2) and drift-control procedures summarized in Section 2.2, to ensure that the observed differences across wave–current and protection cases exceed the instrumentation-level uncertainty. To avoid ambiguity, the wave field in this study is not a directional spectrum with multiple propagation components; it is a unidirectional irregular wave train generated by a piston-type wavemaker. The oblique-wave effect is introduced through a geometric transformation—rotating the pipeline by α relative to the flume axis—so that the measured pressures and pore pressures correspond to an effective oblique-incidence loading condition. This approach captures the key three-dimensional features of the near-field flow separation, circumferential pressure variation, and seabed response around the pipeline, which are central to engineering design. Nevertheless, direction-spreading effects (e.g., short-crestedness, crossing seas) are not reproduced, and the implications of the results should be interpreted within this scope.

3.1. Hydrodynamic Characteristics Around the Pipeline Under the Action of Wave Flow

3.1.1. Analysis of Wave Profile Changes Around Pipelines

During the experiments, four wave height gauges (WHG2123, WHG2124, WHG2126, and WHG2127) were employed to measure water free surface variations in the neighborhood of the submarine pipeline. WHG2123 is positioned on the leeward side of the pipeline, WHG2124 is situated on the seaward side at a greater distance from the pipe, WHG2126 is located directly above the pipeline crown, and WHG2127 is placed on the seaward side in close proximity to the pipe. Figure 6 illustrates the temporal evolution of water surface elevation measured by WHG2123 under the combined action of random waves and currents with varying incident angles. Unlike regular waves, the wave surface of random waves exhibits an obvious randomness and irregularity. The wave-facing area of the pipeline decreases, resulting in a reduced impact from waves. Under downstream random-wave conditions, the wave-surface amplitude decreases, whereas an increase is observed under countercurrent flow. Regarding the influence of incident angle, when $U = -0.24$ m/s, the wave-surface amplitude along the pipeline decreases progressively with increasing incident angle, primarily because the effective interaction area between the incoming waves and the pipeline becomes smaller, leading to a gradual reduction in the measured wave elevation.

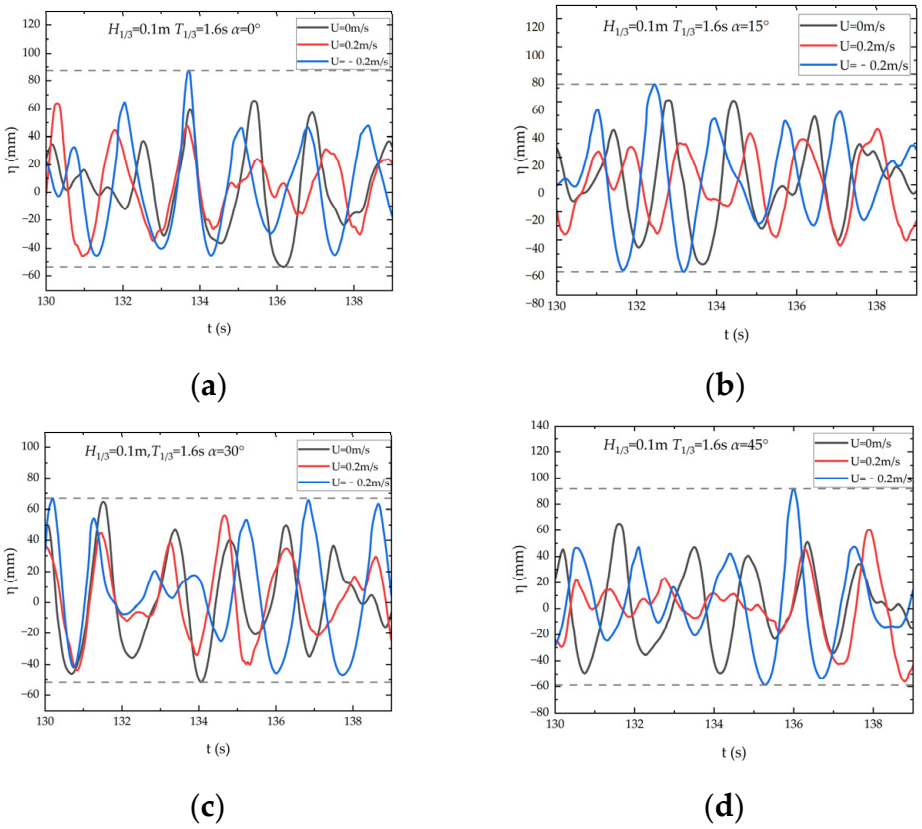


Figure 6. The wave profile at different angles under random waves ($H_{1/3}$ = 0.1 m, $T_{1/3}$ = 1.6 s) with or without currents: (**a**) The incident angle of 0°; (**b**) The incident angle of 15°; (**c**) The incident angle of 30°; (**d**) The incident angle of 45°.

3.1.2. Dynamic Pressure Around the Pipeline

To investigate the dynamic wave pressure acting on the surface of a submarine pipeline, wave pressure sensors numbered Pw1–Pw8 were applied to measure. Pw3 is positioned at the crown of the pipeline, Pw7 is located beneath the pipeline, Pw1, Pw2, and Pw8 are arranged along the upstream (wave-facing) side, and Pw4, Pw5, and Pw6 are situated on the downstream or lee side of the pipeline. Herein, dynamic wave pressure was obtained by subtracting the hydrostatic pressure from the measured total wave pressure.

Figure 7 presents the spatial distribution of dynamic wave pressure under various random wave heights, with a fixed random wave period of $T_{1/3}$ = 1.6 s. As depicted in Figure 7, when waves act independently, the dynamic wave pressure exhibits a positive correlation with wave height; that is, the larger random wave heights induce greater dynamic pressures on the circumference of the pipeline. Figure 7 also illustrates that, under the action of irregular waves with four different incident angles, the dynamic pressure amplitude on the upstream side of the pipeline (i.e., circumferential positions 0–90° and 270–360°) is consistently higher than that on the downstream side (i.e., 90–270°). The dynamic pressure reaches its maximum value at the stagnation point located at 270° around the pipeline. Specifically, for a wave height of $H_{1/3}$ = 0.14 m, the maximum dynamic wave pressures at the 270° stagnation point corresponding to incident angles α = 0°, 15°, 30°, and 45° are 0.93, 0.83, 0.92, and 0.89 kPa, respectively.

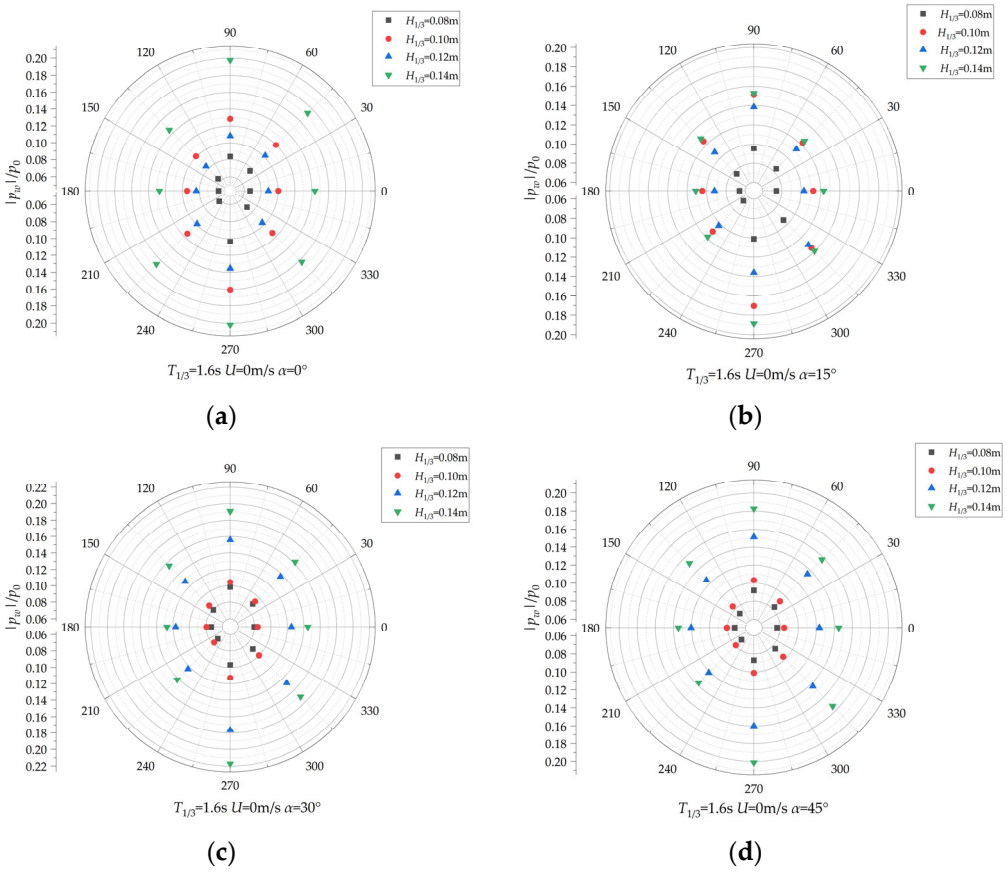


Figure 7. Spatial distribution of maximum dynamic wave pressure around pipelines with different wave height parameters: (**a**) The angle of incidence is 0°; (**b**) The angle of incidence is 15°; (**c**) The angle of incidence is 30°; (**d**) The angle of incidence is 45°.

Moreover, these results demonstrate that, at an incident angle of α = 0°, the dynamic pressure acting on the bottom of the pipeline reaches its highest magnitude, exhibiting a reduction trend with a growing incident angle. As the incident angle increases from 0° to 15°, the maximum instantaneous pore pressure exhibits a decreasing trend, which can be attributed to the reduction in the effective interaction area between the incoming waves and the pipeline surface. When the incident angle further increases from 15° to 45°, vortex shedding becomes increasingly asymmetric, and its lateral displacement becomes more pronounced, progressively influencing the generation and spatial distribution of the maximum instantaneous wave pressure. Although a minor peak emerges within this range of oblique incidence, its magnitude remains lower than that observed under orthogonal wave incidence (α = 0°).

To further clarify the role of wave period in modulating the dynamic pressure on the pipeline surface, Figure 8 presents the spatial distribution of maximum dynamic pressure under a fixed wave height of H1/3 = 0.1 m. The results indicate that the dynamic pressure amplitude increases with wave period, with the most pronounced variations occurring at the pipe crown and invert, and comparatively weaker sensitivity near the 0° (upstream) and 90° (downstream) stagnation points. This is due to the fact that the wave period affects the wavelength and thus the wave number; consequently, a growth trend of the dynamic wave pressure around the circumferential surface of pipelines was witnessed with the rising wave period. For T1/3 = 1.6 s, the maximum dynamic pressures at the 270° stagnation point for incident angles α = 0°, 15°, 30°, and 45° are 0.71, 0.75, 0.51, and 0.45 kPa, respectively, with the peak occurring at α = 15°, consistent with the trends identified for wave-height-induced

loading. Nevertheless, the overall influence of wave period on wave pressure distribution remains weaker than that of wave height.

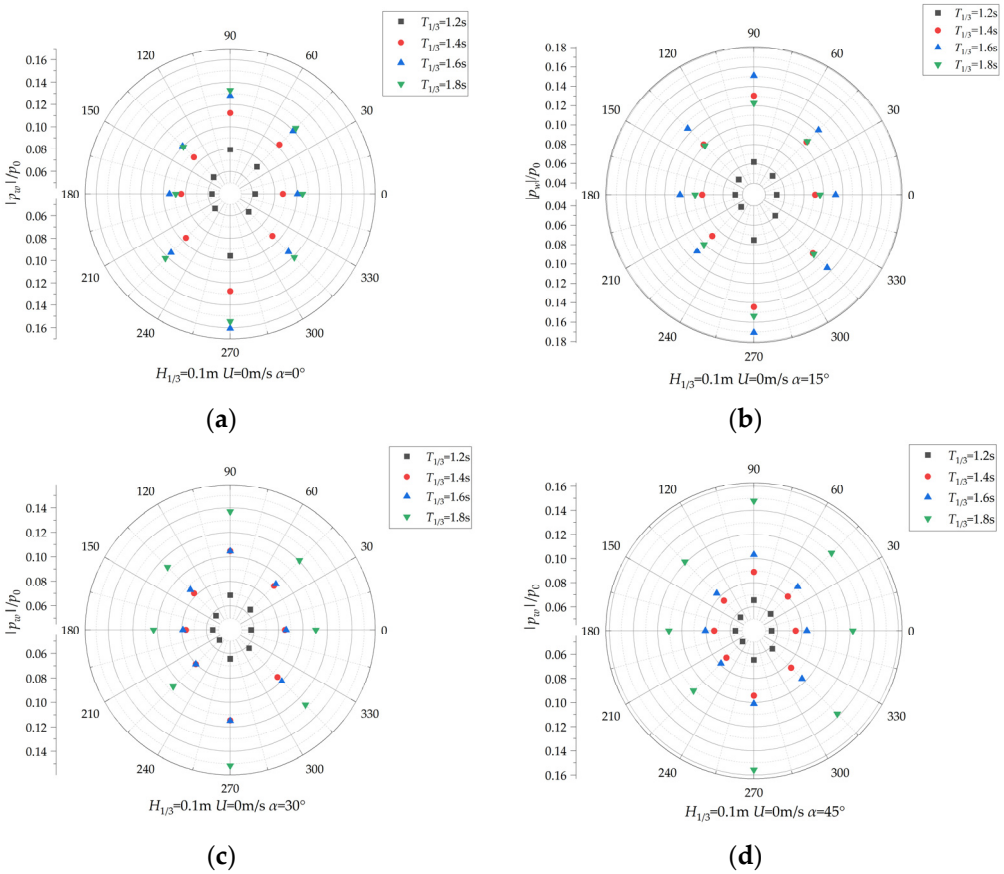


Figure 8. Spatial distribution of maximum dynamic wave pressure around pipelines with different wave period parameters: (**a**) The angle of incidence is 0°; (**b**) The angle of incidence is 15°; (**c**) The angle of incidence is 30°; (**d**) The angle of incidence is 45°.

With increasing wave period, the maximum instantaneous wave pressure acting on the surface of the submarine pipeline exhibits a clear increasing trend. This behavior is primarily attributed to the fact that longer-period waves are associated with larger wavelengths, which significantly enhance both the spatial extent and the duration of orbital motions of near-bed fluid particles. Consequently, the pipeline is subjected to a more sustained and effective hydrodynamic loading within each wave cycle. Meanwhile, the hydrodynamic pressure induced by long-period waves attenuates more slowly with water depth, allowing relatively large pressure amplitudes to be maintained throughout the vertical extent of the pipeline. Furthermore, long-period waves tend to generate a more uniform pressure field around the pipeline, thereby enlarging the effective pressure-bearing area and strengthening the coupling between wave-induced pressure and seabed seepage response. As a result, the wave-pressure amplitude acting on the pipeline surface increases progressively with wave period.

This study examines the influence of ambient flow on dynamic wave pressure acting on a pipeline surface. Figure 9 presents the spatial distribution of dynamic wave pressure under wave–current coupling at varying wave incident angles, under fixed wave height ($H_{1/3}$ = 0.1 m) and period ($T_{1/3}$ = 1.6 s). Overall, the maximum dynamic wave pressure is consistently higher under reverse flow than forward flow, implying more severe hydrodynamic loading when waves propagate against the ambient current. At incident angles of 0°

and 15°, increased flow velocity reduces the maximum dynamic wave pressure. In contrast, at 30° and 45°, the effect of flow velocity on maximum wave pressure is less distinct.

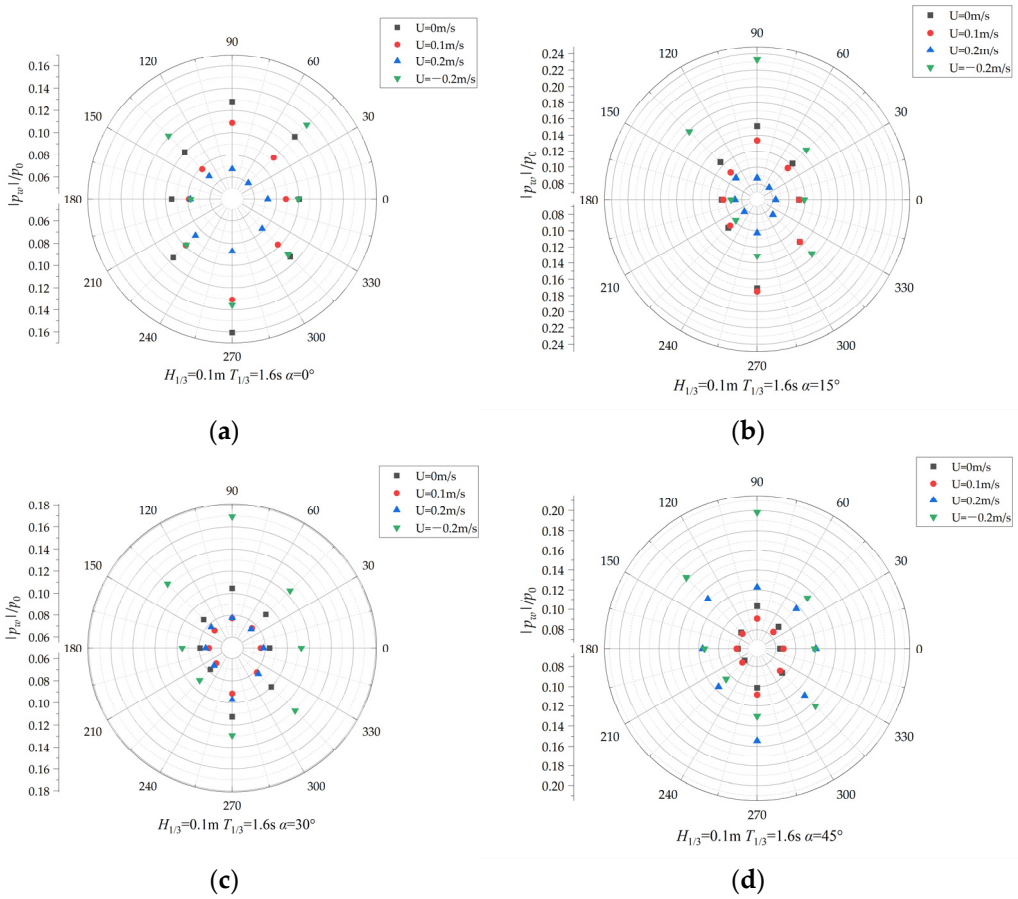


Figure 9. Spatial distribution of maximum dynamic wave pressure around pipelines under different water flow parameters and directions: (**a**) The angle of incidence is 0°; (**b**) The angle of incidence is 15°; (**c**) The angle of incidence is 30°; (**d**) The angle of incidence is 45°.

As background flow velocity rises, the relative speed between waves and the structure decreases, lowering wave-induced particle velocity and acceleration amplitudes. Enhanced bottom boundary-layer dissipation and stabilized flow separation further suppress hydrodynamic fluctuations, leading to a clear decrease in maximum instantaneous dynamic wave pressure. The attenuated pressure variation at 30° and 45° is attributed to the reduced effective area subjected to wave loading, which moderates changes in hydrodynamic pressure.

Under forward flow (e.g., U = 0.2 m/s), dynamic wave pressure amplitudes at the pipeline bottom for α = 0°, 15°, 30°, and 45° are 0.38, 0.45, 0.43, and 0.56 kPa, respectively, indicating the greatest influence at α = 45°. Under reverse flow (U = −0.2 m/s), corresponding values are 0.60, 0.58, 0.57, and 0.57 kPa, showing the strongest impact at α = 0° (waves opposing the current).

3.2. Seabed Dynamic Response Around the Pipeline Under the Wave-Current Action

Figure 10 presents the time-history curves of pore-water pressure within the seabed under different irregular wave conditions. It should be noted that the pore water pressure (p_s) discussed here refers to excess pore pressure, which is obtained by subtracting the static pore pressure. And to better visualize the variations in pore water pressure, the relevant data were non-dimensionalized by the static pore pressure at the seabed surface p_0, obtained by the equation $p_0 = \gamma_w \cdot h$, where γ_w is the specific weight of water and h is

the water depth. Herein, the measurement points p31–p34 presented in the picture are allocated at 3 cm, 6 cm, 12 cm, and 18 cm below the seabed at the center of gravity of the pipeline.

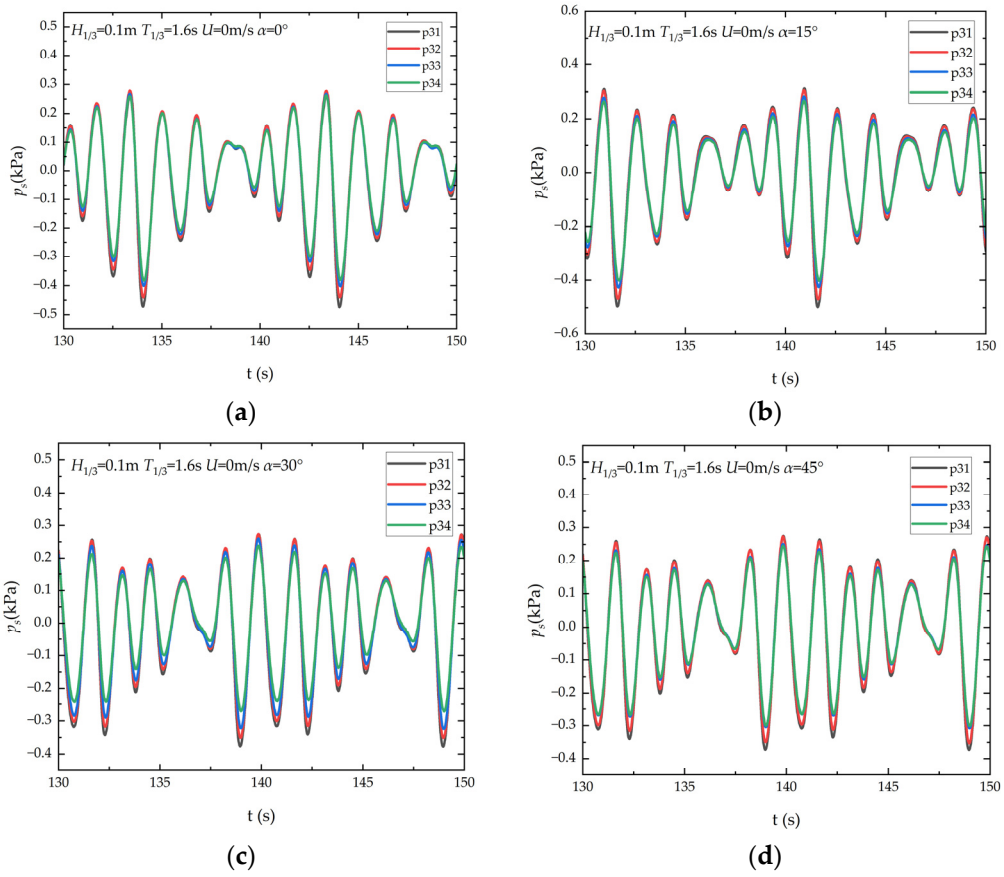


Figure 10. Temporal variation in pressure at the pipeline bottom under a single irregular wave ($H_{1/3}$ = 0.1 m, $T_{1/3}$ = 1.6 s, U = 0 m/s) at various angles: (**a**) The angle of incidence is 0°; (**b**) The angle of incidence is 15°; (**c**) The angle of incidence is 30°; (**d**) The angle of incidence is 45°.

Although Figure 10 shows a 150 s time series, the influence of reflected waves should be considered primarily in relation to the round-trip travel time between the test section and the downstream wave absorber. In this study, the potential reflection-return time can be estimated as $T_r \approx 2\,L/c_g$, where L is the distance from the measurement section to the absorber and c_g is the wave group velocity corresponding to the dominant wave period. Therefore, the portion of the record prior to T_r can be interpreted as being dominated by the incident-wave field, whereas the later portion may contain superposed reflected components. To minimize reflection-induced bias, the quantitative metrics reported in this paper (e.g., representative pore-pressure amplitude and attenuation with depth) were extracted from a pre-reflection analysis window (i.e., a time interval shorter than T_r) and/or based on statistically stable segments in which the reflection coefficient remained small. The full 150 s traces are retained to demonstrate the temporal variability under random wave–current forcing; however, any residual reflections in the late-time segment are expected to mainly affect the detailed waveform rather than the overall comparative conclusions among incident angle, wave–current superposition, sediment size, and protection scenarios.

It can be observed that, due to the unpredictable action of the random wave exerted on the seabed surface, the temporal random fluctuations of the pore water pressure could be witnessed. Also, as depicted in this figure, the pore-water pressure exhibits both amplitude attenuation and phase lag with increasing depth. Taking the incident angle of 0° for instance

(i.e., the wave propagates perpendicular to the alignment of the submarine pipeline), the pore-water pressure amplitudes recorded by sensors p31 and p34 are 0.749 kPa and 0.646 kPa, respectively, with an attenuation rate of 13.75% from p31 to p34. Additionally, the response at p34 lags behind that at p31 by approximately 0.02 s. Under oblique wave incidences of 15°, 30°, and 45°, the pore-water pressure amplitudes measured by p31 are 0.810, 0.651, and 0.649 kPa, respectively, while those at p34 are 0.670, 0.511, and 0.547 kPa, representing reductions of 17.28%, 21.51%, and 15.72%, respectively. The phase lag is 0.02 s. These results clearly demonstrate a decreasing trend in pore-water pressure amplitude with depth, indicating that wave-induced pressure fluctuations attenuate as they propagate downward through the seabed. Furthermore, the observed phase lag between measurements at different depths reflects the time delay in pore-pressure response, attributed to the progressive transmission of wave-induced pressure through the porous seabed medium.

3.3. The Influence of Incident Angles

Figure 11 illustrates the influence of different incident angles on the horizontal distribution of pore water pressure at various positions around the pipeline under wave loading. The pore-pressure amplitude decays rapidly in the vicinity of the pipeline and reaches its maximum on the upstream (wave-facing) side. This attenuation is particularly evident near the seabed surface (e.g., at $z/d = -0.0938$ and $z/d = -0.1875$). Such behavior arises from the wave-damping effect induced by the presence of the pipeline, which disrupts wave propagation and reduces the transmitted pressure fluctuations; consequently, the deeper seabed experiences progressively weaker structural influence. In the upstream region, the pore pressure at locations farther from the pipeline is noticeably smaller than that near the pipe front. This is because the incident waves are forced to intensify upon encountering the pipeline obstruction, producing elevated pore pressures immediately upstream compared with those at more distant locations. Taking the relative depth of $z/d = -0.0938$, for instance, the horizontal attenuation of pore pressure amplitude is particularly significant around the pipeline, with the most significant variations occurring under normal incidence conditions ($\alpha = 0°$). To be more precise, under random-wave alone conditions, the pore pressure amplitude generally exhibits a pattern of 0° and 15° being greater than that of 30° and 45°. These physical results reveal that when the wave travels perpendicular to the axis of the structure, wave propagation is strongly impeded by the pipeline while remaining close to the seabed surface, thereby intensifying the degree of pore pressure fluctuation. This enhancement arises because an oblique wave incidence induces a more pronounced asymmetric flow pattern around the upstream side of the pipeline, thereby intensifying the local velocity gradients and near-bed shear. These strengthened hydrodynamic interactions promote stronger seepage and stress transmission within the underlying sediment, ultimately amplifying the seabed pore-pressure response. While, as the incident angle increases from 0° to 45°, i.e., the direction of wave propagation tends to become parallel to the pipeline axis, the effective interaction area between the incoming waves and the pipeline decreases, and the wave energy dissipation intensity in front of the structure weakens accordingly. This contributes to more wave energy propagates the rear side of the structure, and therefore the pore pressure amplitude in the neighborhood area of the pipeline is reduced. This phenomenon can also be witnessed in other deeper locations ($z/d = -0.1875$, -0.3750, and -0.5625).

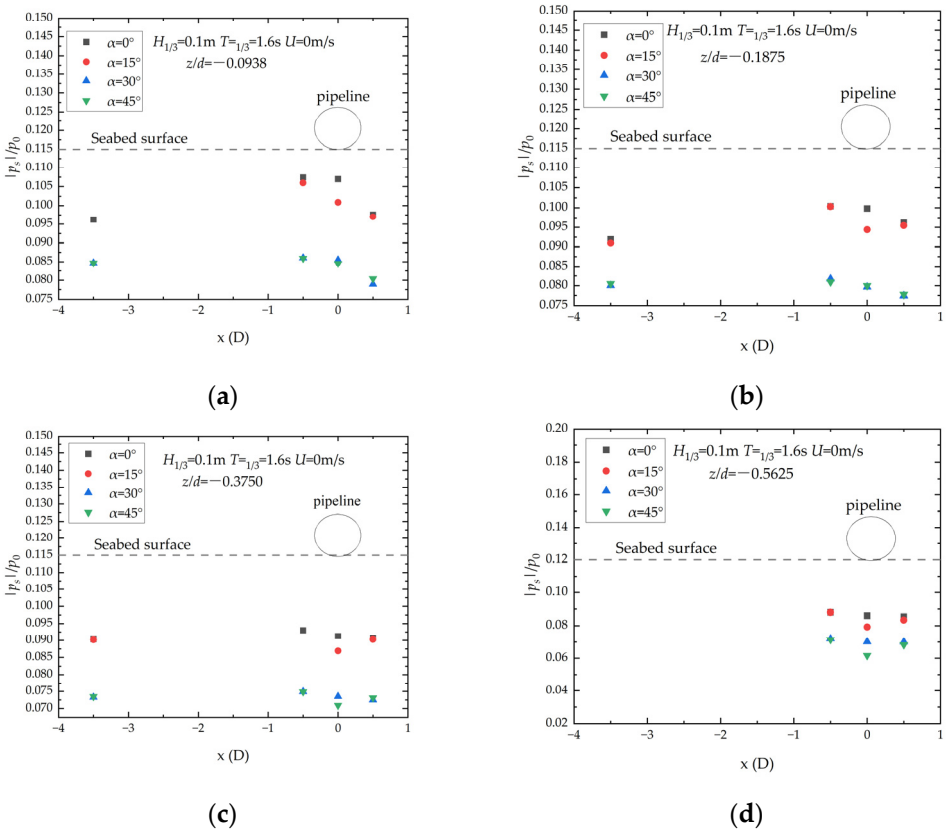


Figure 11. Distribution of pore water pressure along the seabed level at different locations of the pipeline under the action of random waves ($H_{1/3}$ = 0.1 m, $T_{1/3}$ = 1.6 s, U = 0 m/s) with different incidence angles: (**a**) At $z/d = -0.0938$; (**b**) At $z/d = -0.1875$; (**c**) At $z/d = -0.3750$; (**d**) At $z/d = -0.5625$.

3.4. The Influence of Soil Properties

This section examines the effects of sediment particle size on the pore-water pressure response surrounding the pipeline under irregular wave loading at different incident angles ($\alpha = 0°$, 15°, 30°, and 45°). When analyzing the influence of the soil particle diameter, the condition of random wave action alone, i.e., with the current velocity set to 0, was adopted. The random wave height was fixed at 0.1 m, the random wave period at 1.6 s, and four incident angles ($\alpha = 0°$, 15°, 30°, and 45°) were designed for comparison. Further discussion is conducted to evaluate the influence of seabed depth beneath pipelines on the seabed behavior.

Figure 12 presents the depth profile of pore pressure amplitude for various median particle sizes (d50) at a given incident angle. The laboratory results indicate that soils with larger particle sizes have larger pore pressure amplitudes compared with finer sediments. This behavior is primarily attributed to the higher permeability of coarse-grained soils, which allows the periodic dynamic water pressure induced by surface waves to be transmitted more efficiently and rapidly from the seabed surface into the soil interior. As a result, pore water in coarse-grained sediments responds more sensitively to external hydrodynamic loading. In addition, the soil skeleton of coarse-grained materials exhibits relatively higher stiffness, enabling a greater proportion of the incident wave energy to be converted into pore-water pressure rather than being dissipated through soil skeleton deformation. In contrast, fine-grained soils are characterized by lower permeability and restricted pore-water mobility, leading to pronounced attenuation of wave-induced pressure during propagation within the seabed and, consequently, smaller pore-pressure amplitudes. Therefore, under identical experimental conditions, the pore-water pressure

amplitudes developed in coarse-grained soils are consistently larger than those observed in fine-grained soils. Furthermore, the experimental curves demonstrate that the influence of particle size on pore pressure decreases as the wave incident angle increases, with the most pronounced reduction observed at α = 30° and 45°. As the incident angle grows, such as α = 30° and 45°, the wave-blocking effect of the pipeline and the resulting local pressure gradients diminish markedly, leading to weaker dynamic loading of the seabed and a transition of pore pressure into a low-response regime. Under these conditions, the drainage-capacity differences associated with particle size are insufficiently activated, resulting in less pronounced pore pressure contrasts between fine- and coarse-grained sediments. Taking $z/d = -0.0938$ for instance, at the incident angle of 45°, the variation in pore-water pressure between fine- and coarse-grained sediments is up to about 0.4% of p0.

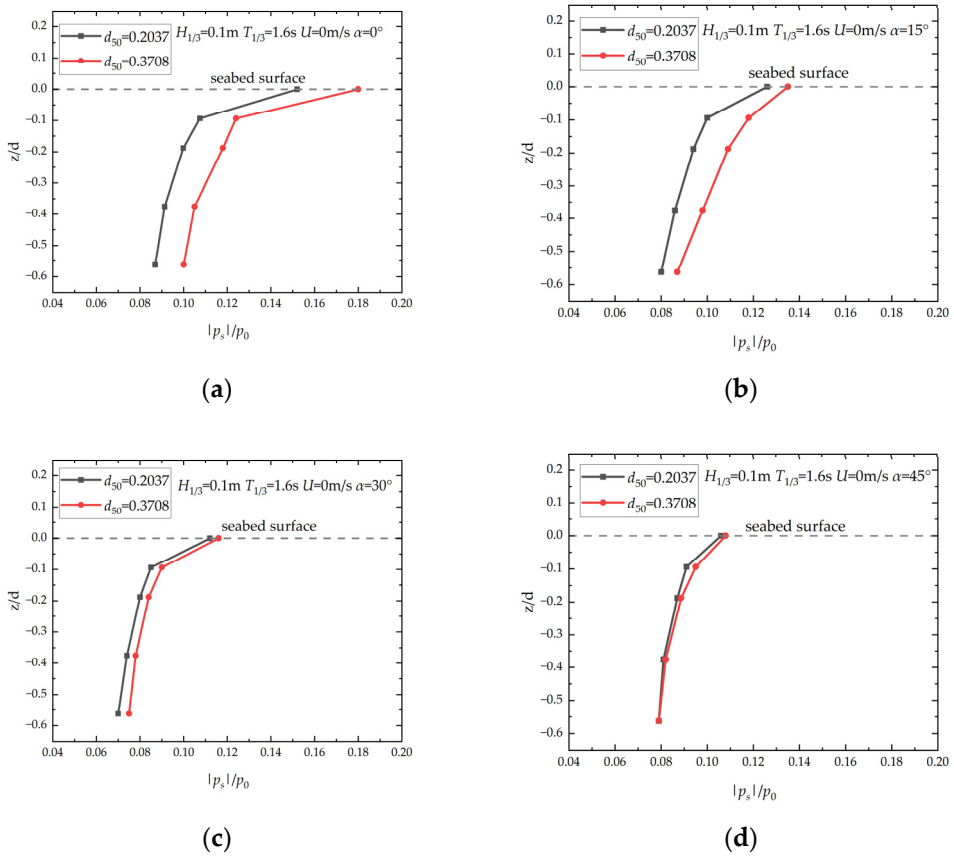


Figure 12. Distribution of pore pressure amplitude along the depth direction in the seabed with different grain sizes under the action of random waves with different incidence angles: (**a**) The angle of incidence is 0°; (**b**) The angle of incidence is 15°; (**c**) The angle of incidence is 30°; (**d**) The angle of incidence is 45°.

Nevertheless, the influence of particle size remains significant between α = 0° and 15°. For example, the variation in pore-water pressure between fine- and coarse-grained sediments is approximately to 1.7% of p_0 for $z/d = -0.0938$ at the incident angle of 45°. This is because the effective pressure-bearing area of the pipeline and the associated flow-structure alterations change only slightly within this angular range. Waves still interact with the pipeline in an approximately normal manner, preserving strong local pressure concentrations and clamping-flow effects. The seabed, therefore, continues to experience strong dynamic excitation, allowing particle-size–dependent permeability differences to be fully manifested, and leading to clear contrasts in pore pressure amplitude across soils of different grain sizes.

3.5. The Influence of Protection Measurements

This section presents the pore pressure responses of two protective measures at four seabed depths (z/d = −0.0938, −0.1875, −0.3750, −0.5625) under the action of a single random wave, as shown in Figure 13. Overall, the results consistently indicate that the geotextile–stone system provides the most pronounced pore-pressure attenuation. The PVC cover exhibits a clear reduction effect in the vicinity of the pipe and within the shallow seabed; however, the pore pressure in the upstream region, farther away from the pipeline, increases compared with the unprotected case.

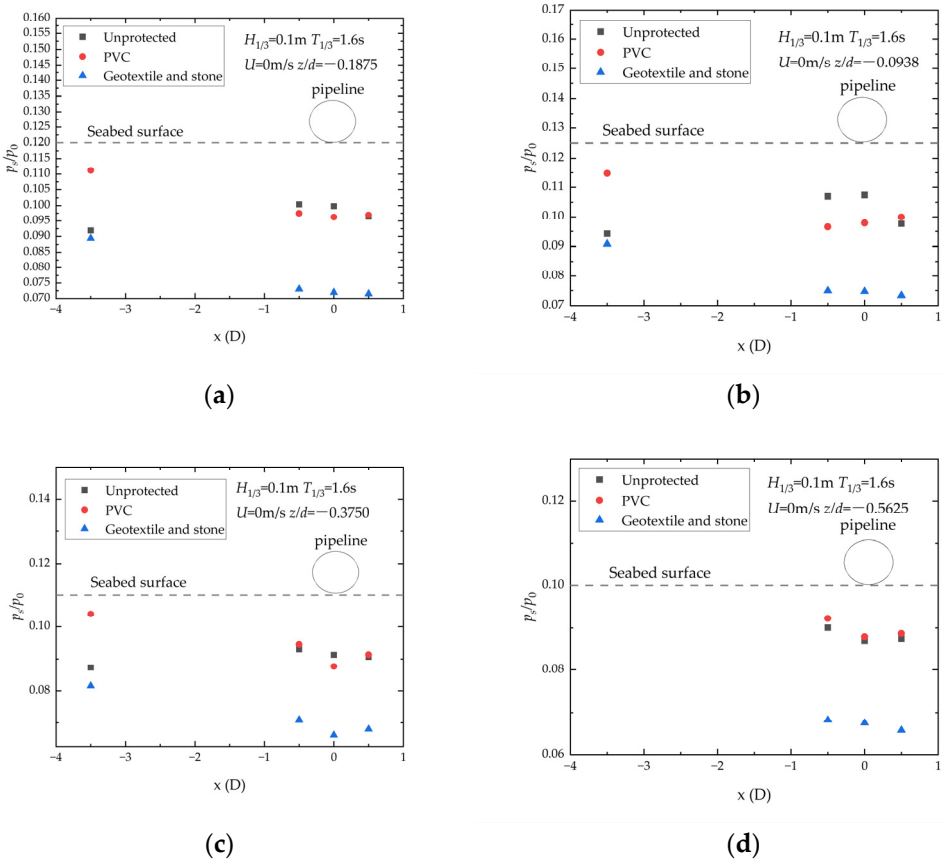


Figure 13. Distribution of submarine pore pressure amplitude along the depth direction for particles of different sizes under random wave action with different protective measures: (**a**) At z/d = −0.0938; (**b**) At z/d = −0.1875; (**c**) At z/d = −0.3750; (**d**) At z/d = −0.5625.

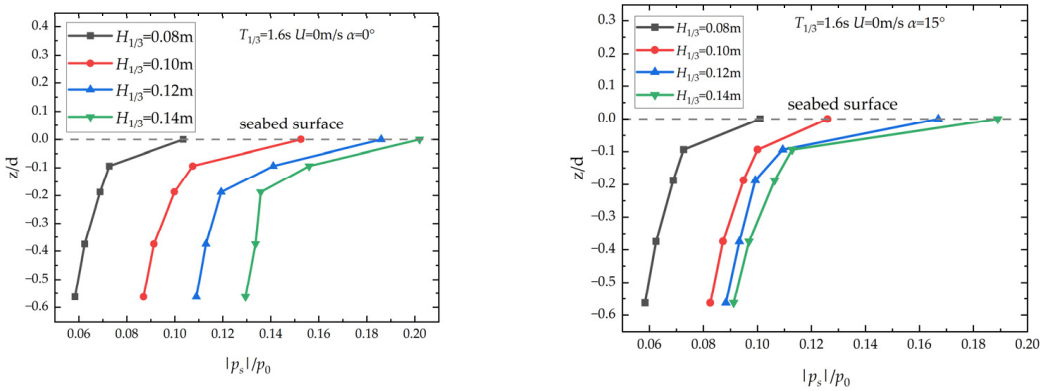
The strong mitigation effect of the geotextile–stone system arises from the combined regulation of wave loading and seabed seepage by the composite protective layer. The geotextile forms a stable and uniform filtration interface on the pipeline surface, inhibiting rapid sand-particle migration and preventing wave-induced pore-pressure fluctuations from being directly transmitted into the natural seabed. Meanwhile, the overlying stone layer, characterized by high porosity and substantial surface roughness, acts as a dissipative porous medium that reduces flow acceleration, attenuates the kinetic energy of wave-induced currents, and markedly decreases the dynamic pressure transmitted to the seabed surface. Furthermore, the composite geotextile–stone structure provides significant load-diffusion and attenuation capability: wave forces acting on the protective surface are redistributed, weakened, and dissipated within the stone layer, and only a low-amplitude, filtered component reaches the underlying sediment. Through this combined "filtration–energy dissipation–diffusion" mechanism, the system effectively suppresses seepage disturbances and reduces the pore-pressure response around the pipeline.

In contrast, the PVC protective cover induces a spatially heterogeneous regulation of the local hydrodynamic and seepage fields. The rigid and smooth PVC surface shields the upper and lower regions of the pipeline, substantially weakening the originally concentrated flow acceleration and dynamic pressure, thereby reducing pore-pressure amplitudes in the near-pipe zone and beneath the pipe. However, the cover also alters the flow pathways: waves encountering the PVC surface are deflected upward and outward, leading to localized flow acceleration and energy convergence at the outer upstream region of the cover. Since this area is not directly shielded, it experiences enhanced hydrodynamic loading caused by diffraction, flow convergence, and accelerated near-bed currents, resulting in a local increase in pore-pressure amplitude away from the pipe. Consequently, under the dual mechanism of "near-field shielding and far-field energy concentration," the PVC cover suppresses pore pressure in the immediate vicinity of the pipeline while amplifying pore pressure in the upstream region farther from the structure.

3.6. The Influence of Wave and Current Parameters

3.6.1. The Influence of Wave Height

To examine the influence of random wave height ($H_{1/3}$) on the pore water pressure in the seabed surrounding pipelines under wave–current interactions with varying incident angles (α = 0°, 15°, 30°, and 45°), Figure 14 illustrates the vertical distribution of the maximum dimensionless pore water pressure at the pipeline bottom ($|p_s|/p_0$) along the normalized seabed depth (z/h) for different wave height conditions. The experimental findings indicate that, under waves of various incident angles, the pore water pressure exhibits a gradual attenuation with increasing seabed depth. The effect of wave height on the pore pressure at the pipeline base is primarily concentrated within the near-surface region (z/h = −0.09 to 0). As wave height is positively correlated with wave energy, the amplitude of seabed pore pressure increases correspondingly with rising wave height, attaining its maximum dimensionless value at the seabed surface (z/h = 0) when $H_{1/3}$ = 0.14 m. The corresponding maximum values are 0.129, 0.091, 0.111, and 0.119 for incident angles of 0°, 15°, 30°, and 45°, respectively.



(**a**) (**b**)

Figure 14. *Cont.*

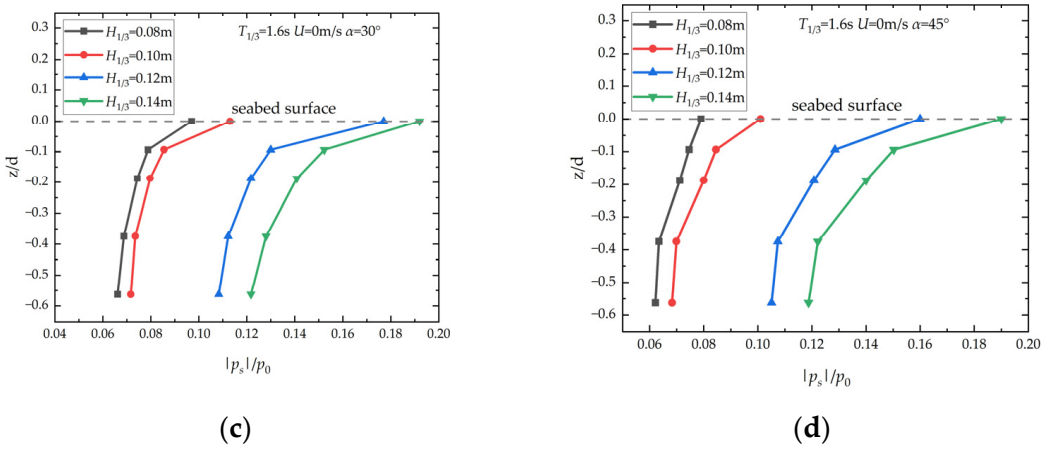


Figure 14. The dimensionless number of pore pressure under different wave height parameters: (**a**) The angle of incidence is 0°; (**b**) The angle of incidence is 15°; (**c**) The angle of incidence is 30°; (**d**) The angle of incidence is 45°.

At the $z/h = -0.09375$, as wave height increases from 0.08 m to 0.14 m in increments of 0.02 m, the amplitude growth rates of pore water pressure at the pipeline bottom under incident angles of 0°, 15°, 30°, and 45° are as follows: 47.54%, 21.57%, and 8.6%; 26%, 31.75%, and 13.86%; 16.49%, 55.75%, and 9.09%; and 27.85%, 58.42%, and 18.75%, respectively. These results demonstrate that the growth rate of pore pressure amplitude under different incident angles generally decreases with increasing wave height. Furthermore, when the incident angle is 45°, the amplitude of pore water pressure at the seabed surface is more significantly influenced by the higher wave height condition ($H_{1/3}$ = 0.14 m) compared to other incident angles.

3.6.2. The Influence of Wave Period

To investigate the influence of random wave period (T1/3) on pore water pressure in the seabed surrounding pipelines under wave action with varying incident angles (α = 0°, 15°, 30°, and 45°), Figure 15 presents the vertical distribution of the maximum dimensionless pore water pressure (ps/p0) at the pipeline bottom along the normalized seabed depth (z/h) for different wave period conditions. The experimental results reveal that, under wave action at various incident angles, the amplitude of pore water pressure near the pipeline base increases with increasing wave period, while exhibiting attenuation with seabed depth. Furthermore, the rate of attenuation decreases as the wave period becomes longer.

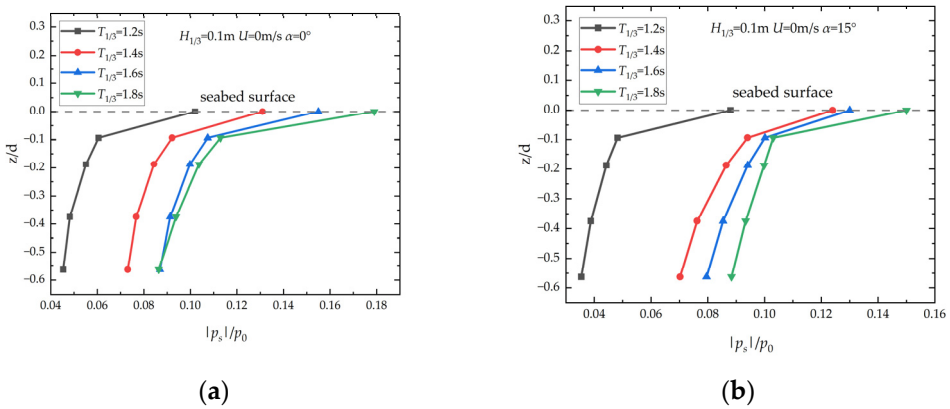
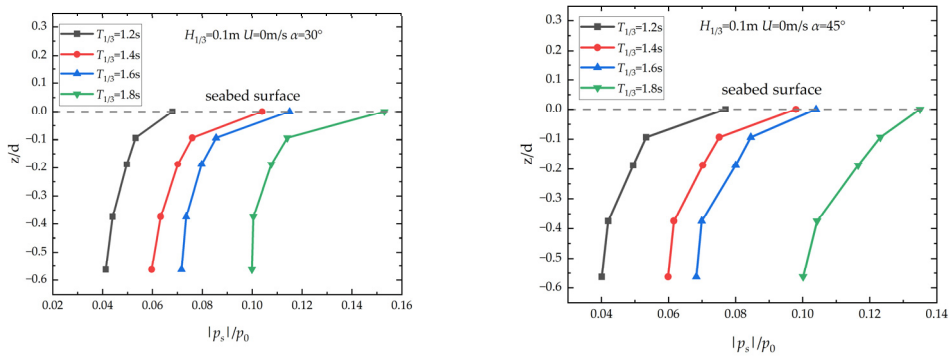


Figure 15. *Cont.*



(**c**) (**d**)

Figure 15. The dimensionless number of pore pressure under different wave cycle parameters: (**a**) The angle of incidence is 0°; (**b**) The angle of incidence is 15°; (**c**) The angle of incidence is 30°; (**d**) The angle of incidence is 45°.

When the wave incident angles are 15°, 30°, and 45°, it is observed that wave periods exceeding 1.6 s led to a reduction in pore pressure amplitude at the seabed surface, which can be attributed to the influence of long-period reflected waves. Similar to the effect of wave height, the impact of wave period on pore pressure at the pipeline base is primarily confined to the near-surface zone (z/h = –0.09 to 0), where the maximum dimensionless pore water pressure occurs at the seabed surface (z/h = 0).

Additionally, the results indicate that the influence of wave period on pore pressure amplitude is significantly weaker than that of wave height. Moreover, for waves with longer periods ($T_{1/3}$ = 1.4–1.6 s) incident perpendicularly (α = 0°), a more pronounced effect on the seabed response around the pipeline is observed. In contrast, when the incident angle exceeds 15°, the influence of wave period on the seabed response becomes considerably diminished.

3.6.3. The Impact of Current Velocity

According to Figure 16, the vertical distribution of the maximum pore water pressure around the three-dimensional pipeline exhibits noticeable variations under different incident angles. In general, for all incident angles, the maximum pore water pressure decreases progressively with increasing seabed depth, and the pore pressure response is mainly concentrated within the shallow seabed layer. This indicates that the combined action of waves and currents predominantly affects the near-surface soil, while the response of deeper soil layers is relatively weak.

When the incident angle is 0°, waves and currents act primarily on the upstream side of the pipeline along the normal direction. Under this condition, the modulation effect of the current on wave propagation is relatively weak, and wave–current energy is rapidly dissipated in front of the pipeline. Consequently, the maximum pore water pressure is mainly concentrated near the seabed surface and attenuates rapidly with increasing depth. This suggests that under normal incidence, the presence of current enhances near-bed shear stress and local wave energy dissipation, but its contribution to the downward transmission of pore water pressure is limited.

As the incident angle increases to 15°, waves and currents gradually form an oblique coupled flow field around the pipeline, and the flow component along the pipeline axis becomes more pronounced. Under the combined wave–current action, the spatial distribution of wave-induced pressure on the upstream side and near the seabed becomes more dispersed. As a result, the overall level of maximum pore water pressure increases, and its attenuation with depth becomes significantly slower than that observed under normal

incidence. This indicates that the presence of current facilitates the transfer of wave energy into the seabed under oblique incidence.

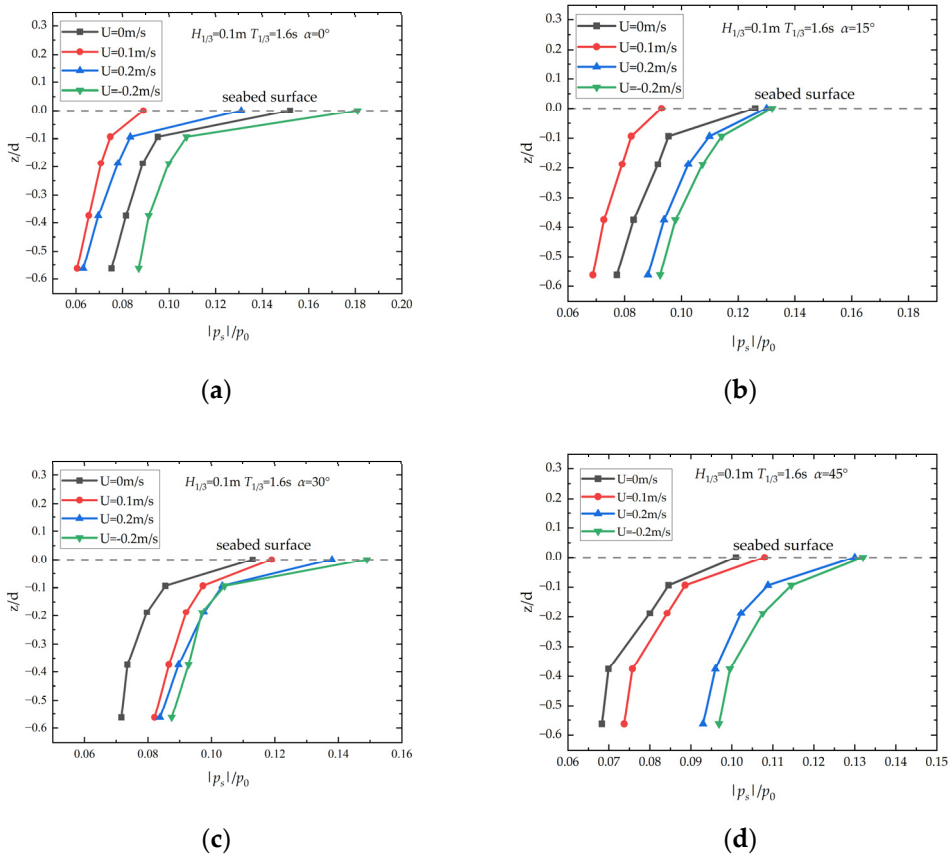


Figure 16. The pore pressure is a dimensionless number with different flow parameters in the main flow: (**a**) The angle of incidence is 0°; (**b**) The angle of incidence is 15°; (**c**) The angle of incidence is 30°; (**d**) The angle of incidence is 45°.

When the incident angle reaches 30°, the wave–current coupling effect is further strengthened, and the three-dimensional flow characteristics around the pipeline become more evident. Influenced by the enhanced current action, near-bed seepage intensity increases, allowing the maximum pore water pressure to remain at a relatively high level within the shallow and intermediate seabed layers and to propagate into deeper regions. Accordingly, the vertical attenuation of pore water pressure is further reduced, demonstrating that the enhancement effect of current on the pore pressure response becomes more significant at moderate incident angles.

At an incident angle of 45°, the flow component along the pipeline direction becomes dominant, and the synergistic interaction between waves and currents reaches its strongest level. The effective duration of fluctuating pressure acting around the pipeline is extended, causing the maximum pore water pressure to attain the highest magnitude among all considered conditions. Moreover, a strong pore pressure response is maintained over a relatively large depth range, with the slowest vertical attenuation rate. This indicates that under large incident angles, the current exerts the strongest promoting effect on both the transmission and accumulation of pore water pressure within the seabed.

For a constant flow condition, a comparative analysis among different incident angles reveals that the maximum seabed pore water pressure around the three-dimensional pipeline generally increases with increasing incident angle, while its attenuation with seabed depth becomes progressively weaker. Under normal incidence, the wave–current interaction is dominated by frontal impact and local energy dissipation, restricting the

influence of pore water pressure primarily to the seabed surface. In contrast, under oblique incidence, waves and currents jointly enhance energy transport along the pipeline axis and within the surrounding flow field, allowing wave-induced pressure to act on the seabed over a longer timescale and thereby extending the depth of pore water pressure influence.

4. Conclusions

This paper investigates the wave profile, dynamic wave pressure and the seabed response around a subsea pipeline through flume experiments under the combined action of random waves and currents. The pore pressures of the seabed around the pipeline at different angles relative to the direction of wave propagation, soil properties, and protection measurements were comprehensively compared. Based on the statistical analysis of the laboratory results, the conclusion is drawn as follows:

1. The random wave profile is inherently random, and the addition of current increases the randomness of the wave surface. The dynamic wave pressure is significantly influenced by wave height, wave period, and current velocity. As these parameters increase, the dynamic wave pressure also increases, indicating a positive correlation.
2. The pore pressure induced by wave (and current) loads decreases as well as delays continuously with seabed depth increases, and those damping rates also decrease with the increasing seabed depth. Additionally, as wave height, wave period, and current velocity increase, pore pressure increases.
3. Under the combined oblique waves and currents loadings, small-angle wave incidence (0–15°) produces limited variations in pore-pressure amplitude, whereas larger incidence angles (15–45°) lead to notably damped pore-pressure amplitudes compared with orthogonal wave incidence, thus suppressing the seabed response around the underlying pipeline. From an engineering perspective, particular attention should therefore be given to waves incident orthogonally to the pipeline, as these conditions are more conducive to seabed liquefaction and may pose increased risk to pipeline stability.
4. The pore water pressure on the seabed of soil with a large particle size is larger than that of soil with a small particle size. This is mainly due to the large permeability coefficient of coarse-grained soil, which makes the periodic hydrodynamic pressure of waves on the seabed surface more fully and rapidly transmitted to the soil, and the response of pore water to external loads more sensitive.
5. As a protective system, the geotextile–stone cover provides a more comprehensive and effective reduction in pore-water pressure around the pipeline. This measure attenuates wave-induced pressure over a wider spatial range and offers stronger overall protection. In contrast, the PVC cover primarily reduces pore pressure in the immediate vicinity of the pipeline—namely, at the upstream face and beneath the pipe—while the pore pressure in the upstream region farther from the pipeline increases due to flow deflection and localized energy convergence. Moreover, the effectiveness of both protective measures diminishes with increasing seabed depth, indicating that the shielding effect becomes less pronounced in deeper soil layers.

Author Contributions: Conceptualization, D.-S.J., K.S. and L.C.; methodology, K.S. and L.C.; formal analysis, D.C., W.S., D.L., M.L. and Z.W.; investigation, D.C., W.S., D.L., M.L. and Z.W.; resources, D.-S.J., K.S., L.C. and D.W.; data curation, D.C., W.S., D.L., M.L. and Z.W.; writing—original draft preparation, W.S.; writing—review and editing, D.-S.J., K.S. and R.W.; visualization, W.S.; supervision, D.-S.J., K.S. and L.C.; project administration, D.-S.J. and K.S.; funding acquisition, D.-S.J.; validation, D.W. All authors have read and agreed to the published version of the manuscript.

Funding: This research received no external funding.

Data Availability Statement: The experimental data are available upon request to the corresponding author.

Conflicts of Interest: Author Dejian Wei was employed by Pinglu Canal Group Co., Ltd., Nanning, 530201, China. The remaining authors declare that the research was conducted in the absence of any commercial or financial relationships that could be construed as a potential conflict of interest.

References

1. Fredsoe, J.; Sumer, B.M. *Hydrodynamics Around Cylindrical Structures*; World Scientific: Singapore, 1997.
2. Herbich, J.B. *Offshore Pipe Design Elements*; Marcel Dekker Inc.: New York, NY, USA, 1981.
3. Jas, E.; O'Brien, D.; Fricke, R.; Gillen, A.; Cheng, L.; White, D.; Palmer, A. Pipe stability revisited. *J. Pipe Eng.* **2012**, *12*, 259–268.
4. Xiao, X.; Feng, X.; Jiang, J. Pore Pressure Response and Scour around Vibrating Pipelines in Silty Seabed under Wave Loading: Laboratory Flume Study. *J. China Univ. Pet. (Nat. Sci. Ed.)* **2021**, *45*, 133–141.
5. Chen, H.; Zhang, J.; Tong, L.; Sun, K.; Guo, Y.; Wei, C. Experimental study of soil responses around a pipeline in a sandy seabed under wave-current load. *Appl. Ocean. Res.* **2023**, *130*, 103409. [CrossRef]
6. Zhang, Q.; Zhou, X.; Ye, G. Wave Load Induced Seabed Response and Liquefaction Analysis Around Pipelines with Different Burial Depths. *J. Shanghai Jiao Tong Univ.* **2021**, *55*, 489–496. [CrossRef]
7. Luo, Y. Study on Seabed Stability Around Submarine Pipelines Under Wave Load Action. Master's Thesis, Southwest Jiaotong University, Chengdu, China, 2019. [CrossRef]
8. Dong, L. Wave-Induced Pore Pressure Dynamic Response Test Study on Layered Seabed. Master's Thesis, Chongqing Jiaotong University, Chongqing, China, 2024. [CrossRef]
9. Sun, K.; Zhang, J.; Gao, Y.; Jeng, D.-S.; Guo, Y.; Liang, Z. Laboratory experimental study of ocean waves propagating over a partially buried pipeline in a trench layer. *Ocean. Eng.* **2019**, *173*, 617–627. [CrossRef]
10. Gao, Y.; Zhang, J.; Tong, L.; Guo, Y.; Lam, D. Wave induced silty seabed response around a trenched pipeline. *Ocean. Eng.* **2022**, *245*, 110527. [CrossRef]
11. Xu, Y.; Cui, L.; Jeng, D.-S.; Wang, M.; Sun, K.; Chen, B. Hydrodynamic characteristics around offshore pipelines and oscillatory pore pressures in sand beds under combined random wave and current loads. *Theor. Appl. Mech. Lett.* **2025**, *15*, 100575. [CrossRef]
12. Wu, S.; Jeng, D.S. Effects of dynamic soil permeability on the wave-induced seabed response around a buried pipeline. *Ocean. Eng.* **2019**, *186*, 106132. [CrossRef]
13. Liu, X.; Li, Q.; Liao, Z. Analysis of the characteristics and mechanisms of seabed response around buried pipelines considering wave-Induced pore-pressure accumulation and stress-coupling effects. *J. Eng. Geol./Gongcheng Dizhi Xuebao* **2021**, *29*, 1770–1778. [CrossRef]
14. Satrio, D.; Putra, D.J.; Dhanistha, W.L.; Utama, I.K.A.P.; Putranto, T.; Hayati, N.; Muharja, M.; Madi, M. Numerical Study of the Effect of Depth Immersion and Rotation Direction on the Performance Cross-Flow Savonius Turbine. *Pomorstvo* **2024**, *38*, 250–262. [CrossRef]
15. Dhaifullah, M.H.; Jifaturrohman, M.I.; Putranto, T.; Setyawan, D.; Utama, I.K.A.P.; Huang, L. Enhancing pure oscillatory response motion performance: Innovative designs for semi-submersible and catamaran floating photovoltaic systems (FPVs) in various sea-state conditions. In *Proceedings of the 2024 International Conference on Sustainable Energy: Energy Transition and Net-Zero Climate Future (ICUE), Pattaya City, Thailand, 21–23 October 2024*; IEEE: New York, NY, USA, 2024; pp. 1–6.
16. Yu, P.; Hu, R.; Zhang, J.; Yang, Q.; Zhao, J.; Cao, L.; Zhu, C. Numerical study on local scour characteristics around submarine pipelines in the Yellow River Delta silty sandy soil under waves and currents. *Deep. Undergr. Sci. Eng.* **2024**, *3*, 182–196. [CrossRef]
17. Zhu, F.; Ye, Y.; Huang, P. Numerical simulation study on seabed erosion and deposition near the Zhoushan Cezi Island Zhenhai submarine pipeline. *Oceanogr. Res.* **2014**, *32*, 74–81.
18. Shi, S. Numerical Simulation of Three-Dimensional Scouring of Submarine Pipelines. Master's Thesis, Shanghai Jiao Tong University, Shanghai, China, 2019. [CrossRef]
19. Zhao, K.; Wang, Q.; Chen, S.; Zhuang, H.; Chen, G. Dynamic response of pipelines in liquefiable seabed under nature loadings: Waves and currents. *Ocean. Eng.* **2021**, *230*, 109051. [CrossRef]
20. Sun, K.; Gao, Y.; Zhang, J. Seabed Response Around a Partially Buried Pipeline Subjected to the Combined Ocean Waves and Currents Loads in a Trench Layer. In *Proceedings of the International Conference on Offshore Mechanics and Arctic Engineering, Singapore, 9–14 June 2024*; American Society of Mechanical Engineers: New York, NY, USA, 2024; Volume 87837, p. V05BT06A039.
21. Ma, H.; Li, B.; Zhang, S. Scour mechanism around a pipeline under different current-wave conditions using the CFD-DEM coupling model. *Comput. Geotech.* **2024**, *170*, 106304. [CrossRef]
22. Hu, K.; Bai, X.; Vaz, M.A. Numerical simulation on the local scour processing and influencing factors of submarine pipeline. *J. Mar. Sci. Eng.* **2023**, *11*, 234. [CrossRef]

23. Li, Y.; Fuhrman, D.R. CFD simulation of nonlinear deep-water wave instabilities involving wave breaking. In *Proceedings of the International Conference on Offshore Mechanics and Arctic Engineering, Online, 21–30 June 2021*; American Society of Mechanical Engineers: New York, NY, USA, 2021; Volume 85161, p. V006T06A065.
24. Si, W.; Wang, M.; Gao, Y.; Sun, K.; Chen, B.; Wang, R.; Cui, L.; Jeng, D.-S.; Zhao, H. Experimental Study of Submarine Pipeline with Geotextile and Stone Cover Protection Under the Superposition of Waves and Currents. *J. Mar. Sci. Eng.* **2024**, *12*, 2218. [CrossRef]
25. Whitehouse, R. *Scour at Marine Structures: A Manual for Practical Applications*; Thomas Telford: Westerkirk, Scotland, 1998.
26. Cheng, L.; Yeow, K.; Zang, Z.; Li, F. 3D scour below pipelines under waves and combined waves and currents. *Coast. Eng.* **2014**, *83*, 137–149. [CrossRef]
27. Lin, M.Y.; Wang, L.J. Seepage Force on a Buried Submarine Pipeline Induced by a Solitary Wave. *J. Mar. Sci. Eng.* **2020**, *8*, 324. [CrossRef]
28. Neelamani, S.; Al-Banaa, K. An approach to estimate the optimal depth of burial of crude oil pipelines for different marine conditions in Kuwait. *J. Eng. Res.* **2014**, *2*, 13. [CrossRef]
29. Fredsoe, J.; Sumer, B.M. *The Mechanics of Scour in the Marine Environment*; World Scientific Publishing Company: Singapore, 2002.
30. Zhang, X.L.; Jeng, D.S.; Luan, M.T. Dynamic response of a porous seabed around pipeline under three-dimensional wave loading. *Soil Dyn. Earthq. Eng.* **2011**, *31*, 785–791. [CrossRef]

Disclaimer/Publisher's Note: The statements, opinions and data contained in all publications are solely those of the individual author(s) and contributor(s) and not of MDPI and/or the editor(s). MDPI and/or the editor(s) disclaim responsibility for any injury to people or property resulting from any ideas, methods, instructions or products referred to in the content.